The Moon before mare

Adrien Broquet, J. Andrews-Hanna

The Moon before mare

A. Broquet[1], J. C. Andrews-Hanna[1]

[1]Lunar and Planetary Laboratory, University of Arizona, Tucson, AZ 85721, USA

Corresponding author: Adrien Broquet (adrien.broquet@arizona.edu)

Abstract

The crust of the Moon experienced a unique geodynamic evolution, beginning with its crystallization from a magma ocean, continuing through a period of heavy impact bombardment, and followed by extensive basaltic mare volcanism. All these events have left crucial records imprinted in the form of topographic features and gravity anomalies. Here, we invert gravity and topography data using a two-layer thin-shell loading model under the premise of pre-mare isostasy to investigate the global structure of the crust and solve for feldspathic crust and mare thickness, together with mare-induced flexure. The tectonic record and partially buried crater population are used to constrain the bulk of mare volcanism to have been emplaced on a 40 km elastic lithosphere, although mare within large impact basins may have formed on a thinner elastic lithosphere. The mare thickness and associated flexure are removed to calculate a map of the surface and crust of the Moon before mare volcanism. The pre-mare surface in the western Procellarum region is found to be ~2 kilometers lower than the surrounding nearside, and several possible explanations, including a giant impact, pore space annealing, isostatic adjustment, and crustal erosion induced by a mantle plume or thermal anomaly, are discussed. The pre-mare elevation map further sheds light on the ring structure of Imbrium, which is seen to resemble that of Orientale. Imbrium's outermost ring is observed to be at a larger radial distance to the northeast relative to the south, indicating that some level of lithospheric variability affected ring formation at the time of impact. The western part of Imbrium's ring within Oceanus Procellarum is not found in the pre-mare topography, implying that it either never formed or that some processes erased its signature from gravity and topography. The feldspathic, pre-mare, crust is found to be ~7 km thinner within large nearside basins than in models not accounting for the high-density mare. The pre-fill floor of these basins was ~6 km deeper than currently observed, and together with their updated crustal structure, these new insights have implications for impact simulations that try to reproduce the crustal structure of nearside mare basins.

1. Introduction

The terrestrial planets and the Moon have experienced intense and widespread volcanism that have shaped their surfaces and crusts. Volcanic products on the Moon are dominantly expressed in the form of dark deposits covering much of the nearside. These deposits, called maria, consist of effusive iron-rich basaltic plains that are thought to be the result of partial melting in the mantle and subsequent upward propagation of that melt through dikes (e.g., Wilson & Head, 2017; Head & Wilson, 2017). Crater counting statistics on exposed mare units suggest that the peak formation age for the surface units occurred during the late Imbrian period (~3.8–3.6 Ga; Hiesinger et al., 2011). Mare materials cover about 17% of the lunar surface, making these deposits a substantial component of the upper crust (Head & Wilson, 1992).

Knowing the lateral variations in mare thickness is crucial to understand the structure of both large nearside impact basins and the enigmatic Procellarum KREEP Terrane (PKT) region that is thought to have played a prominent role in the thermal evolution of the Moon (Laneuville et al., 2013). The volume of mare material further provides fundamental information on melting in the lunar mantle, which is an important constraint for early geological history and thermal evolution (Shearer et al., 2006). In addition, although mare materials contribute to a significant fraction of the nearside crust, no model has been presented to investigate the global structure of the Moon before mare materials obscured the surface, including the pre-mare topography and the thickness of the felspathic crust. Both would have implications for the early geologic history of

the Moon, including the formation of the large nearside basins, the dynamics of magma ascent, and the formation of the lunar asymmetries.

A variety of approaches have been used to probe the structure and volume of the maria. Geological analyses of volcanically embayed craters found mare thicknesses generally less than 1.5 km outside of the major impact basins (e.g., De Hon, 1979; Du et al., 2019). Gravitational evidence for buried craters was used to obtain thicknesses of 1.5 km over most of the PKT region based on the inferred burial of the crater rims (Evans et al., 2016). Using a localized analysis of gravity spectra, western PKT mare thicknesses were found to range from 0.1 to 6 km, with an average of 0.7 km (Gong et al., 2016). An alternative model mapped lateral variations in mare thickness using global gravity and topography and obtained mean mare thicknesses of about 1.6 km over the mare region, but higher average values of >4 km over the largest impact basins (Andrews-Hanna et al., 2014). Williams & Zuber (1998) compared the predicted large nearside basin depths to observations and obtained mare thicknesses of up to 5 km there (see also Head, 1982). Investigations of the flexural response to the maria as constrained by the tectonic signature of these large basins indicated the possibility of much thicker maria within the basins, with estimated thicknesses of 5 to 10 km (Solomon & Head, 1980; Freed et al., 2001).

The above studies each used very different approaches and, surprisingly, arrived at similar mean values but different and sometimes contradictory maps of mare thickness. These studies further suffered from several limitations. For example, constraints based on buried or partially buried craters (De Hon, 1979; Evans et al., 2016; Du et al., 2019) rely on sparse data, often only provide a bound on mare thickness, and are not applicable in the thickest mare accumulations. Flexure was neglected in the study of both Williams & Zuber (1998) and Andrews-Hanna et al. (2014), which would cause mare thickness to be underestimated within and close to impact basins. Finally, the work of Solomon and Head (1980) used a number of simplifications to describe the mare load and was only able to estimate the mare thickness within major impact basins. What is needed is a mare thickness model based on laterally continuous data, built upon robust assumptions, and that accounts for the flexural response to the mare loading.

Some of the lunar maria, known as cryptomare, do not exhibit the characteristic albedo difference relative to the highlands as a result of an overlying layer of feldspathic impact ejecta (Whitten & Head, 2015; Sori et al., 2016). Using a mare flooding model, the thicknesses of some cryptomaria were found to range from 0.5 to 4 km, with the thickest deposits being located within large impact basins, such as Smythii (Whitten & Head, 2015). However, this model did not account for lithospheric flexure and thus provides only a lower bound on mare thickness. In another study, two different gravity investigations were used to infer the thickness of cryptomare materials on a global scale and found average values of about 2.5 to 6.3 km (Sori et al., 2016). The higher estimate is based on an analysis of filtered Bouguer gravity, which may misattribute some regions of thinner crust as being associated with cryptomare. The lower estimate is based on an alternative approach analyzing gravity anomalies relative to the expected isostatic gravity field, and should thus be less biased by crustal thickness variations.

Although mare volcanism featured prominently in the geologic evolution of the Moon, the volume and distribution of the maria remain poorly constrained. In this study, we use gravity and topography together with a loading model to determine lateral variations in mare thickness and to reconstruct maps of the Moon before mare volcanism. This model constrains the thickness of the mare loads, based on the premise that the pre-mare crust was likely isostatically

compensated, and considering the deflections of the lithosphere in response to the mare loading. In the first section, we describe our modelling approach to invert gravity and topography data and discuss additional constraints on mare thickness based on surface tectonics and partially buried craters. Next, we present maps of mare thickness for different lithosphere elastic thickness. Thicknesses and volumes of the maria for various assumed crustal structures, in comparison to other extrusive and intrusive materials, together with the implications of our mare thickness map for the mode of emplacement of mare basalts are discussed in detail in a companion paper (Broquet & Andrews-Hanna, 2023a). Mare thickness and flexure are used to construct models of the feldspathic crust thickness and pre-mare surface elevation. These models are used to shed light on the origin of the PKT surface depression, the ring system around Imbrium, and the crustal structure of large nearside impact basins.

2 Methods

2.1 A two-step two-layer inversion of gravity and topography

Lateral variations in mare thickness are investigated by expanding upon the two-layer global inversion of gravity and topography data by Andrews-Hanna et al. (2014). Our new approach makes use of a thin-shell model (Banerdt et al., 1986; Broquet, 2022a; Broquet & Andrews-Hanna, 2022) that partitions the crust into a mare top load, a feldspathic top and bottom load, and the associated lithospheric displacement that exactly reproduce the observed gravity and topography (Appendix A). Importantly, given two knowns, it is possible to solve for only two unknowns. In the original formulation of the model, known gravity and topography were inverted for crustal top and bottom loads in an evenly determined inversion (Banerdt et al., 1986). As our model considers an additional unknown associated with the mare top load, the inversion problem becomes under-determined and one more assumption is required.

Given that the lunar crust is thought to be the result of the solidification of a floatation crust following a global magma ocean (e.g., Wood et al., 1970), the crustal roots should have initially been in the isostatic ratio with the crustal surface loads (see also Searls et al., 2006; Ritzer & Hauck, 2009). Subsequent crustal modifications include the formation of impact basins. However, while some large mascon gravity anomalies exist apart from mare fill, the nearside basins lack the characteristic sub-isostatic annulus found on these non-mare mascons (Andrews-Hanna, 2013; Melosh et al., 2013). The overall lack of this crustal annulus in the nearside has been interpreted to be due to significant relaxation for the nearside basins in the warm PKT region (see Ding & Zhu, 2022). Thus, a reasonable starting assumption is that the crust in the nearside was approximately isostatic prior to volcanic loading but then was depressed downward by the mare load (see also Wieczorek & Phillips, 1999). To evenly determine the two-layer loading model, the bottom loads in the feldspathic crust are therefore assumed to be in an equal pressure isostatic ratio (see Dahlen, 1982; Hemingway & Matsuyama, 2017, see equation A2) with the feldspathic crust top loads, leaving the mare top load and isostatically compensated feldspathic top load as the two unknowns (Searls et al., 2006).

Based on the assumption of pre-mare isostasy, our model solves for the thickness of the maria, the thickness of the feldspathic crust, and the resultant flexure from the net load that exactly matches the observed gravity and topography. Following Wieczorek et al. (2013), only models with non-negative crustal thicknesses are accepted. We note that, as in classical crustal thickness inversions, our model solves for the relief along the mare-crust interface, but cannot

determine the mean radius of that interface. If the mean radius of that interface were set equal to the mean planetary radius, half of the planet would have positive mare thicknesses by definition in a spherical harmonic analysis. The mean radius of the mare-crust interface is thus varied such that the distribution of positive mare thickness approximately matches the observed mare distribution (see below). Outside of the mare regions, the modeled mare thickness is not physically meaningful and may include predictions of negative mare thickness. For that reason, we adopt a two-step approach to constrain lateral variations in the thickness of the maria.

In our first step model, the long-wavelength (degree < 90) top and bottom loads in the feldspathic crust are constrained to be in the equal pressure isostatic ratio, with a second independent top load of basaltic mare material as described above. Although the bulk of the feldspathic crust formed early when the crust was hot and weak (Wood et al., 1970), surface modifications by smaller scale processes such as impacts later in time may have induced significant departures from isostasy at higher degrees and shorter wavelengths, with a local support of geological loads by the lunar lithosphere. For example, pre-mare impact craters are expected to generate local mare thickening with associated gravity anomalies (Evans et al., 2016), but should not affect the crust-mantle interface. Thus, from degree 90 to 150 the model transitions to having no bottom loads (where the gravity and topography are a result of variations in mare thicknesses and crustal top loads) using a cosine taper. A cosine taper was here used instead of the minimum-amplitude filter (Wieczorek et al., 2013) in order to transition to 100% top loading at a specified degree. This transition beyond degree 90 was chosen to reflect the lithospheric degree of compensation, where for an elastic thickness of 15 km appropriate for the early lunar lithosphere (Matsuyama et al., 2021), the topography is dominantly supported by the lithosphere. The mare model is tapered to zero between degrees 350 and 500 to prevent ringing. We note that the exact shape and extent of this latter filter has no influence on the conclusions presented in this work. Finally, the mean radius of the mare-crust interface is iterated in 100 m increments to meet the condition that 90% of the mare region has non-negative mare thickness (see section 3.2).

In a second step, the previously output mare thickness is thresholded to a minimum value of zero and then clipped to the observed mare and cryptomare distribution (Nelson et al., 2014; Whitten & Head, 2015). The updated mare thickness is then input into a new model as a known load, allowing us to solve for the independent (no longer isostatic in non-mare regions) top and bottom loads in the feldspathic crust required to exactly match the observed gravity and topography. This model doesn't require any further assumptions and uses a minimum amplitude downward continuation filter with an amplitude of 0.5 at degree 90 to damp the oscillations of the crust-mantle interface relief (see also Wieczorek et al., 2013). The result is a self-consistent model of mare and crustal thickness matching the expectation for an approximately isostatic long-wavelength pre-mare crust and a flexurally supported mare load, and that reproduces previous crustal thickness inversions in non-mare regions (e.g., Wieczorek et al., 2013).

However, the assumptions in this approach are not valid for the small maria outside of the main nearside mare region. Gravity analyses of Orientale and other farside basins suggest that they formed in a non-isostatic state, which led to the flexural uplift of the sub-isostatic annuli and basin centers following basin formation (Andrews-Hanna et al., 2013; Melosh et al., 2013; Freed et al., 2014; Johnson et al., 2016). Given the similar negative free-air annulus around Moscoviense, the same process may have occurred there. For these basins, the positive free-air gravity anomalies in the basin centers are dominantly not due to the mare loading. Furthermore,

within the South Pole-Aitken basin, maria are expressed in the form of small isolated patches. As a result, our global inversion may not accurately represent the maria in that area. For these reasons, we have decided to treat the mare within Orientale, Moscoviense, and the South Pole-Aitken basins separately. Following geologic estimates, we set the mare thickness within these basins to 200 m in the step 1 mare thickness model prior to the step 2 model of crustal thickness (Whitten et al., 2011, Pasckert et al., 2018).

In the present framework, contributions from the long-wavelength fossil figure of the Moon (Garrick-Bethell et al., 2010; Matsuyama et al., 2021) constitute a known long-wavelength departure from isostasy that would incorrectly affect the derived mare thickness. We have adopted the formulation of Garrick-Bethell et al. (2010) with minor corrections (see Appendix B) to compute the lunar fossil figure, and the resulting $C_{2,0}$ and $C_{2,2}$ contributions of the fossil figure (-85 and 84 m instead of -114 and 111 m) are removed from observed gravity and topography before the inversion. We note that this correction also affects our strain estimations that are relevant to the following section, as this approach removes strains originating from the lunar figure. However, we found that these long-wavelength ancient strains have no effects on the much later and localized basin tectonics investigated below.

Several parameters influence the outputs of our mare and crust inversion, including the elastic thickness of the lithosphere (T_e), which controls the amount of mare-induced flexure, the assumption of pre-mare isostasy, the density of the mare and crust, and the assumed average crustal thickness. The elastic thickness of the lithosphere is varied from 20 to 80 km (e.g., Solomon & Head, 1980; Freed et al., 2001; Mohit & Phillips, 2006), with the results tested against both constraints from the tectonic record and from mare thickness estimates based on partially buried craters, as discussed below. Elastic thicknesses less than 20 km would imply heat flows with values in excess of 120 mW m^{-2} (T_e = 10 km; Broquet, 2022b) that are two times higher than expected at the time of mare emplacement (Laneuville et al., 2013). On the other hand, elastic thicknesses greater than 80 km would suggest heat flows less than 20 mW m^{-2} (T_e = 90 km) that are much lower than expected. Young's modulus and Poisson's ratio are assumed to be 100 GPa and 0.25, respectively, following previous lunar lithospheric flexure studies (e.g., Solomon & Head, 1980). The effect of varying the isostatic transition filters is tested with two additional inversions (60–120 and 110–170 instead of 90–150), and the isostatic ratio is varied from sub-isostatic (0.9) to super-isostatic (1.1; see equation A2). The mean global crustal thickness is ranged from 35 to 45 km, and the density of the feldspathic crust is considered to range from 2550 to 2750 kg m^{-3}, where the high upper limit allows for the possibility that the porosity is lower beneath the lunar maria (Wieczorek et al., 2013). Finally, following gravity analyses (Goossens et al., 2020) and density measurements (Kiefer et al., 2012), the bulk density of the mare is varied from 2850 to 3150 kg m^{-3}. Although higher bulk densities are measured for hand samples, we note that those bulk density measurements may overestimate the true bulk density of the maria at the kilometer scale due to the absence of macro-scale porosity within them (e.g., porous interflow zones). In addition, analyses of radar sounding data found evidence for regolith layers interbedded between successive mare flows (Ono et al., 2009) and the presence of these high-porosity layers would also decrease the bulk density of the maria. For these reasons, our preferred model will use a mare density of 2850 kg m^{-3} (Goossens et al., 2020), though higher densities will also be tested. Although these values may not cover the full range of possible density and porosity arrangements in the subsurface, these latter parameters

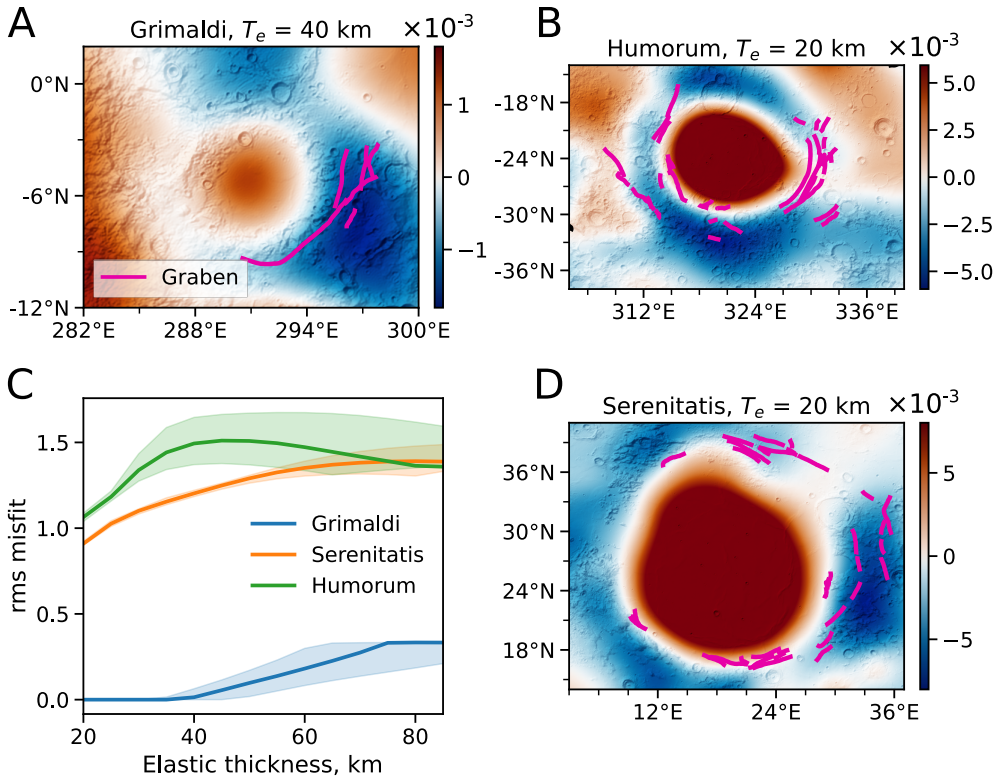

Figure 1: Predicted areal strains at Grimaldi (A), Humorum (B), and Serenitatis (D) for elastic thicknesses as noted in the image title (see also Figures S1-S2-S3-S4). (C) rms misfit comparing the modeled strain to the tectonic record as a function of elastic thickness. Negative strains indicate extension. Solid lines are for the nominal model, where the strain map is thresholded to 5×10^{-4} and the shaded give the rms misfit for thresholds of 2.5 to 7.5×10^{-4}. Most colormaps used in this study are from Crameri (2018).

have minor effects on mare thickness and volume compared to the elastic thickness of the lithosphere, as discussed below.

2.2 Constraints based on the tectonic record

Tectonic landforms may provide the most relevant record of the geodynamic evolution of mare loading and hold clues to the structure of the mare and crust. Tectonics are driven by stresses in the lithosphere, which primarily depend on the elastic thickness of the lithosphere at the time of loading (Solomon & Head, 1980; Freed et al., 2001). Several nearside basins, including Mare Humorum, Serenitatis, and Grimaldi are surrounded by extensive (>250 km) linear to arcuate rilles, which are graben-like features that testify of mare-induced extension (Figure 1). Although a large population of compressional wrinkle ridges is also found in the nearside maria (Watters & Johnson, 2010), lunar graben are more diagnostic of the lithosphere thickness at the time of mare loading owing to their position outside of the basins within narrow zones of flexural extension. The observed graben population was previously used together with a loading mare model to constrain the elastic thickness of the lithosphere to be less than 25 km for Grimaldi and 40–50 km for Serenitatis and Humorum (Solomon & Head, 1980). However, it was noted that this model had a sign error for the membrane stresses in the lithosphere, which

affected the inferred elastic thicknesses (Freed et al., 2001). A more detailed finite element model constrained the elastic thickness at Serenitatis to be 25 km when linear rilles formed, lower than found in Solomon & Head (1980), and to have increased to 75 km at the time of wrinkle ridge formation (Freed et al., 2001). These models, however, used a number of simplifications to describe the mare load, and a reanalysis of mare-induced strains is warranted.

Our model described above outputs lithosphere displacements, which can be used to calculate lithospheric strains (see Broquet & Andrews-Hanna, 2022; 2023b). The formation of arcuate rilles or graben requires horizontal extension, and both should preferentially form where loading strains are largest. Horizontal extension is achieved with a negative areal strain, which is obtained by adding the sum of principal horizontal strains and their product. All strains are evaluated at the surface. In order to constrain the elastic thickness of the lithosphere, we compare the normalized areal strain to the tectonic record. To ensure that loading strains would be sufficient to drive graben formation, the modeled extensional (negative) strains are first thresholded to a minimum value of 2.5 to 7.5×10^{-4}, which is slightly lower than that recorded by lunar graben (e.g., Watters & Johnson, 2010; Callihan & Klimczak, 2019). This strain range of 2.5 to 7.5×10^{-4} is also representative of a frictional yield stress at 5–15 km depth in the crust, assuming a Young's modulus of 80 GPa. Strains are then normalized with respect to their absolute maximum tensile values within the investigated area in order for our model to be representative of the local crustal structure. Each observed tectonic feature is digitized into equidistant points (Fortezzo et al., 2020), and we then calculate the rms difference between the normalized strain map (maximum value of 1) and the tectonic map (with a value of 1 at each graben) at the graben locations as a function of lithosphere elastic thickness. This approach favors models in which tectonic features are found in areas of peak strain, while strongly disfavoring models in which tectonic features are found in areas with strains opposite or less than that expressed in that tectonism.

2.3 Constraints based on partially buried craters and basins

Geologic observations of craters within the maria hold crucial constraints on the local thickness of mare deposits outside of major impact basins. For craters partially buried by mare, the pre-mare rim height from scaling laws has been compared to the observed height in order to infer the thickness of the surrounding mare (e.g., De Hon, 1979). However, these estimates come with some caveats, including that the investigated impact crater may be sitting on top of earlier mare materials, which implies that the inferred mare thickness is only a lower bound. For example, partially buried crater rims are found within both the Imbrium and Humorum basins where the actual mare thickness must be much greater than indicated by the crater rim heights (De Hon 1979). The number of similar partially buried craters that formed on earlier mare surfaces elsewhere is unknown. An additional issue comes from crater degradation processes, which can reduce the rim height of a crater and thus artificially increase the thickness of a mare deposit if not corrected for. In that case, the mare thickness estimate from a degraded partially buried crater is an upper bound. Such issues have been tackled by modelling crater degradation processes (Du et al., 2019), but these analyses were only performed on a few impact craters, making these a sparse constraint on the thickness of the lunar maria. Alternatively, craters that fully excavated the mare, characterized by a low FeO concentration in the ejecta indicating excavation of the Moon's underlying anorthositic crust, can also be used to provide an upper bound on mare thickness (e.g., Thomson et al., 2009). Unfortunately, these craters are also scarce, making them a relatively poor constraint on the global thickness of the mare. Finally, we

note that mare thickness estimates from partially buried craters could suffer from an addition bias. Exposed crater rims will preferentially be found at local high points in mare basement where the mare is thinnest, and this would thus bias mare thickness estimates toward thinner values.

For these reasons, direct comparisons between mare thicknesses based on crater morphology and global gravity and topography inversions have to be carefully made. Here, we use mare thickness estimates from partially buried craters, which are the most abundant, from previous studies (De Hon, 1974, 1979; De Hon & Waskom, 1976; Thomson et al., 2009; Du et al., 2019). We treat these as lower bounds because in some instances the craters may have formed on pre-existing mare and then been partially buried by subsequent mare eruptions as discussed above, and some of these craters are fully buried "ghost craters" for which the overlying mare thickness is unknown. We note that crater degradation could lead to an overestimation of these local mare thicknesses in the earlier databases, but this effect has been shown to affect the thickness estimate only moderately (~100 m, Du et al., 2019). In total, we make use of 309 lower-bound mare thickness estimates that are well scattered across the nearside maria and that have average and standard deviation thicknesses of 500±360 m with a full range of 100 to 1900 m. The elastic thickness of the lithosphere is the dominant control on mare thickness, and this parameter is varied to maximize the number of locations where lower bound estimates on the mare thickness are satisfied.

Although craters confirmed to have formed in the pre-mare crust and for which degradation was modeled are sparse, they can be used to provide reliable local constraints on the thickness of the maria. We make use of the absolute mare thickness from Du et al. (2019) that were estimated at 25 crater locations that have a rim composition consistent with highland materials and for which crater degradation was considered. At these locals, the mean mare thickness and standard deviations are 190±130 m and thicknesses range from 70 to 720 m. We assume that the mare thickness constraints from Du et al (2019) are fully representative of the mare thickness at the crater locations. These constraints are used in an inverse distance weighting, normalized to a characteristic distance of 75 km chosen to represent the typical scale of mare thickness variations in our model, to locally refine our nominal global mare thickness maps. We note that the exact characteristic distance has no effect on the conclusions of this study.

The deep structure of large impact basins also holds clues to the thermo-mechanical properties and composition of the lithosphere (e.g., Miljković et al., 2016). Our model constrains the thickness of the feldspathic crust, which is obtained after having corrected for mare thickness. The amount of felspathic crustal thinning is proportional to the Bouguer anomaly contrast and has been observed to be linearly correlated with the basin size (Neumann et al., 2015). Several parameters that directly affect the modeled thinning of the feldspathic crust are here explored, including the elastic thickness of the lithosphere and density contrast between mare, crust, and mantle materials. The amount of feldspathic crustal thinning is estimated for several large basins (diameter greater than 150 km) from the difference between an azimuthal average far from (1.8× crater radius away) and within (< 100 km) the basin center, and comparisons between the near and farside are made. Most farside impact basins are heavily degraded and relatively smaller in diameter than those on the nearside. For that reason, our nearside/farside comparison focuses on Orientale, which is well preserved, relatively unaffected by the maria, and the largest farside basin after the South Pole-Aitken basin (Neumann et al.,

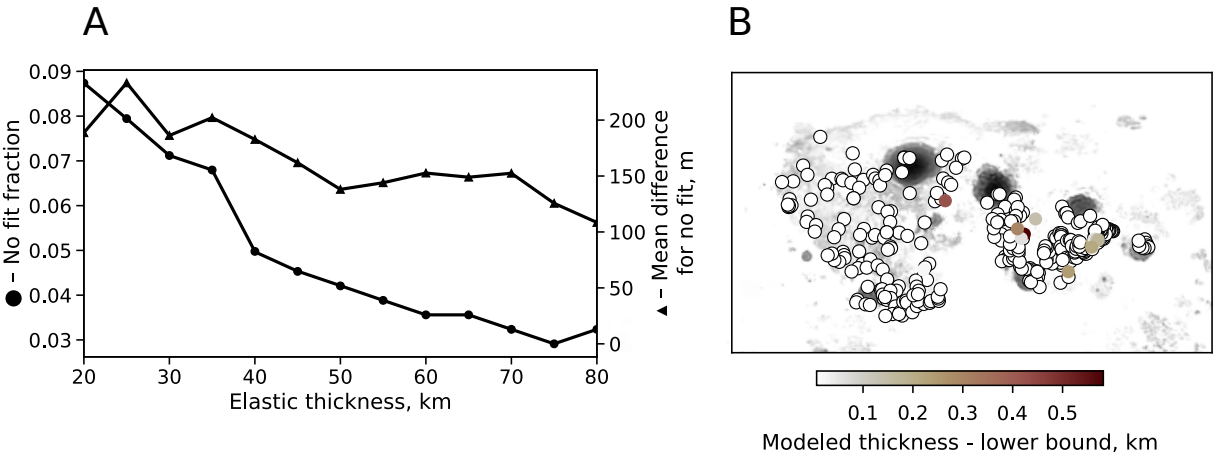

Figure 2: (A) Fraction of the mare thickness lower bounds that do not satisfy our mare model as a function of elastic thickness (dots, left axis, N=309). The lower bounds of mare thickness are derived from multiple sources: De Hon (1974, 1979) and De Hon & Waskom (1976) with N = 287; Thomson et al. (2009) with N = 10; and Du et al. (2019) with N = 12. Mean difference between our model and the mare thickness estimates at the locations where the lower bound is not satisfied as a function of elastic thickness (triangle, right axis). (B) Gray-shaded context mare thickness map overlain by mare thickness lower bound locations where the color indicates the difference between our model and the local constraint assuming an elastic thickness of 40 km. White fill with a black contour indicates the lower bound is satisfied.

2015). The crustal structure of Orientale is scaled and compared to that of the nearside Humorum, Smythii, Nectaris, Crisium, Serenitatis, and Imbrium basins for various assumed crustal structures.

3 Results and discussion

3.1 The elastic thickness of the lithosphere at the time of mare emplacement

Our areal strain predictions are compared to the arcuate rille systems surrounding Humorum, Serenitatis, and Grimaldi. For elastic thicknesses less than or equal to 20, 20, and 40 km for Humorum, Serenitatis, and Grimaldi, respectively, the mare loading model predicts local extension where most of the rilles occur (Figure 1; a global strain map is shown in Figure S1). For Grimaldi, the nominal tectonic model with a strain threshold of 5×10^{-4} favors elastic thickness of less than or equal to 40 km, before the misfit starts to drastically increase (Figure S2). For strain thresholds of 2.5 and 7.5×10^{-4}, this maximum elastic thickness ranges from 45 to 35 km, respectively. For both Humorum and Serenitatis, low elastic thicknesses are found to better fit the tectonic record for all strain thresholds (Figures S3-S4). Although thinner still elastic lithospheres may further reduce the misfit for Serenitatis and Humorum, the implied heat flows with values of 120 mW m^{-2} for T_e = 10 km are two times higher than expected at the time of mare emplacement (Laneuville et al., 2013), and constraints from buried craters favor thicker lithospheres as discussed below. We have tested the sensitivity of our strain maps to other parameters, including the mare and crust densities, and found that variations of these parameters had limited effects on our strain estimates (<5%) compared to that of the elastic thickness of the

lithosphere. Together, these constraints suggest relatively thin elastic lithospheres (≤ 40 km) during the bulk of mare emplacement within these basins.

In a second approach, we compare our mare thickness estimate to the lower bounds based on previous analyses of partially buried craters (De Hon, 1974, 1979; De Hon & Waskom, 1976; Thomson et al., 2009; Du et al., 2019). The misfit is estimated using two parameters. One gives the fraction of the locations that satisfy partially buried crater constraints. The second quantifies the mean difference between our model and the partially buried crater constraint for those locals that did not satisfy the lower bound. For all analyses, the mare thickness is estimated from an inverse distance-weighted average of all estimates within a 75 km radius away from the partially buried crater (the exact distance-weighting does not influence the main results). This analysis first demonstrates that our mare thickness inversions are consistent with more than 90% of the partially buried crater estimates (Figure 2). The misfit as a function of elastic thickness is also seen to be relatively flat. The reason is that lithospheric flexure, and thus elastic thickness, has little influence on mare thickness away from thick mare accumulations that are mostly found within large basins. Nevertheless, elastic thicknesses of 40 km and higher provide a better fit and satisfy >95% of the lower bound estimates based on partially buried craters (Figure 2). For these high elastic thicknesses (≥ 40 km), the mean difference is also minimized. However, we note that the mean difference is dominated by only a small number of craters located at the edge of the mare units where the modeled mare thickness necessarily tapers to zero due to the nature of the spherical harmonic model. Contrary to the tectonic analysis, elastic thicknesses of less than 30 km are less consistent with the crater constraints and obtain higher misfit, where for an elastic thickness of 20 km, only 91% of the crater constraints are satisfied.

Given that the tectonic analysis favors elastic thicknesses of less than or equal to 40 km, and the analysis based on crater morphology suggests elastic thicknesses of 40 km and higher, elastic thicknesses of 40 km appear to be most representative of the bulk of the mare emplacement. We note that the difference in elastic thickness constraints based on basin tectonics favoring thinner lithospheres and based on partially buried craters favoring thicker lithospheres could be due to the basin-forming impact events having excavated most of the crust and lithosphere (Freed et al., 2014) provided that the bulk of the mare thickness was emplaced prior to thermal re-equilibration (~100 Myrs). In addition to mare loading, there are a variety of processes that were not modeled and that could play an important role in affecting surface tectonics and hence our estimated elastic thickness. These include pre-existing zones of weaknesses associated with the collapse of the transient cavity (Johnson et al., 2016), dike induced faulting (Klimczak, 2014), or the effect of lithosphere-scale thrust faults bordering the central mascons (Byrne et al., 2015). Loading associated with the sub-isostatic annulus of an impact basin (Andrews-Hanna, 2013) would also induce significant extensional strains close to the inner ring without requiring an overly thin elastic lithosphere. This is clearly illustrated by looking at predicted strains for the Orientale basin, where loading of the crustal annulus induces a zone of extension close to the Inner Rook, consistent with observed graben systems, for all tested elastic thicknesses (Figure S1). A thick sub-isostatic annulus around large nearside basins could have loaded the lithosphere at the time of mare eruption and graben formation and then relaxed away due to the higher heat flow in the PKT region (see Ding & Zhu, 2022).

Nevertheless, our preferred 40 km elastic thickness is consistent with earlier work that used the tectonic record (Solomon and Head, 1980; Freed et al., 2001) and viscoelastic relaxation models (Mohit & Phillips, 2006). Modeled temperature variations in the mantle can also be used

399 to infer the elastic thickness of the lithosphere. Thermal evolution simulations suggest the depth
400 to the Curie temperature of iron metal (~1050 K) in the PKT region to have ranged from ~20–30
401 km at the time of mare volcanism (Laneuville et al., 2018). This isotherm is close to that at the
402 base of the lithosphere for typical lunar dry diabase and olivine rheologies (Mohit & Phillips,
403 2006), suggesting elastic thicknesses in the range of ~20–30 km at the onset of mare volcanism
404 and increasing to 30–80 km at about 3 Ga (Laneuville et al., 2018), which is also consistent with
405 our work. Finally, we emphasize that the input elastic thickness of the lithosphere does not affect
406 our crustal thickness estimates outside of the mare regions where lithospheric displacements are
407 not investigated.
408

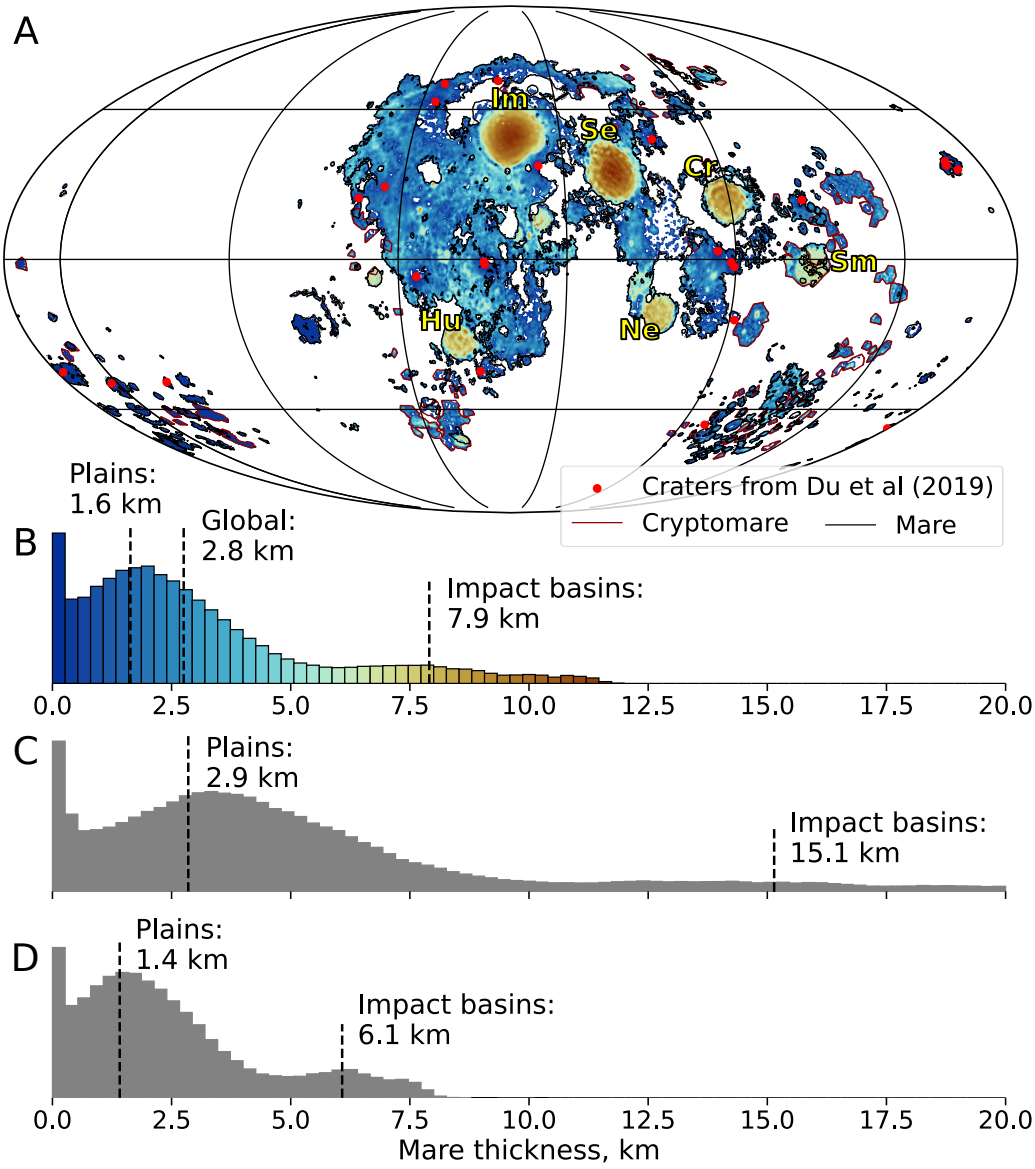

Figure 3: (A) Mollweide projection centered on 340°E of the nominal global mare thickness model with an elastic thickness of 40 km. The color-scale is shown in (B). The mare and cryptomare contours are from Nelson et al. (2014), and Whitten & Head (2015), respectively, and the red circles indicates the location of the 25 mare thickness estimates from Du et al (2019). (B) Color-coded histogram of the estimated area-weighted mare thickness, with mean thicknesses for the plains, impact basins, and on a global scale. (C-D) Histograms of mare thickness assuming an elastic thickness of 20 km (C) and 60 km (D).

3.2 Mare thickness

Lateral variations in mare thickness are obtained from our two-layer inversion of global gravity (Konopliv et al., 2014) and topography (Smith et al., 2010), corrected for the fossil figure (Appendix B), after having thresholded mare thicknesses to zero and spatially clipped the mare

map to known mare and cryptomare regions. The results presented below do not depend on the gravity field model. We also note that the fossil figure correction leads to a local mare thickness decrease of about 500 m in the center of the PKT region, which is ~5 times lower than the global mare thickness average. However, due to the nature of this $C_{2,0}$–$C_{2,2}$ structure (increase in the outer PKT, decrease in the inner PKT) and our adjustment of the reference height of mare-crust interface to match the mare distribution, this correction has only a minor effect on the mean mare thicknesses. Based on our fit to the tectonic record and partially buried crater population, the nominal model assumes an elastic thickness of 40 km, but models with elastic thicknesses of 20 and 60 km are presented for comparison purposes. As discussed above, this 40 km value is consistent with earlier work that also investigated the tectonic record (Solomon and Head, 1980; Freed et al., 2001) and with independent thermal evolution models of the Moon (Laneuville et al., 2013). In order for the mare thickness to be positive in most of the mare region (~90% of the mare surface area), the mare-crust interface for the nominal model is referenced to a radius of 1.9 km below the mean planetary radius, which is consistent with the average elevation of the mare surface of -2 km. This 90% value was chosen based on the minimum of the gradient of the function defining the area covered by mare from the reference radius, which reflects where increasing the radius has the least impact on increasing the positive mare area. Following previous gravity analyses, our nominal model further uses a crustal density and thickness of 2550 kg m^{-3} and 40 km, and a mare density of 2850 kg m^{-3} (Goossens et al., 2020).

The mare map displays important spatial variations (Figure 3), with an average thickness and standard deviation of 2.8±2.5 km, for a total mare volume of ~2.0×10^7 km^3. The thickest mare deposits are found at the center of the large nearside basins, with maximum thicknesses of about 11 km within Serenitatis or Imbrium, and with average values of 7.9±1.6 km across all nearside basins with diameters greater than 350 km. Mare thickness in the plains outside of these basins is significantly lower, where we find an average of 1.6±1.4 km. In this model, we have also added local constraints on mare thickness from 25 partially buried craters for which degradation was modeled (Du et al., 2019), as discussed in Section 2. We note that these local constraints only slightly affect the local mare thickness, but have no implications for both the global mare distribution and thickness. A mare thickness model based only on gravity and topography without inclusion of the crater constraints is also included as a Supplementary Data File. For elastic thicknesses of 20 and 60 km, our mare thickness maps also exhibit similar bimodal distributions with a large concentration within impact basins (Figure 3C-D). However, the global mean value, the averages within the plains and major impact basins vary substantially. For example, for the thin lithosphere case, the mean mare thickness within impact basins would be as high as 15 km, and for the thicker lithosphere the thickness would be 6 km. This demonstrates the effect of the mare load on lithospheric flexure, where thin lithospheres lead to greater mare thicknesses.

We have further explored the effect of crustal and mare density and mean crustal thickness on our inversion. We found that thicker crusts (45 km instead of 40 km) and smaller density contrasts between the mare and crust (100 kg m^{-3} instead of 300 kg m^{-3}) did not change the overall mare distribution, but increased the average mare thickness by at most 15%. On the other hand, thinner crusts (35 km) and higher density contrasts (600 kg m^{-3}) decreased the average mare thickness by at most 20%. One reason for these minor differences lies in our iterative approach, which estimates the radius of the mare-crust interface based on a criterion to obtain non-negative mare thicknesses over 90% of the known mare area. In that framework, any long-wavelength effects on the mare thickness, such as from the assumed density structure of the

subsurface, are partially offset by the resultant change to the mean mare-crust interface radius. We also considered how slight departures from long-wavelength isostasy would affect the overall mare distribution with four additional inversions. In two inversions, we assumed that the Moon was in a state of early super- and sub-isostasy, in which we scale the thickness of the bottom loads in the feldspathic crust by ×0.9 and ×1.1 relative to their isostatic values, respectively. One other inversion assumed that full isostasy is maintained up to degree 110 before smoothly transitioning to no bottom loads at degree 170 (instead of 90–150 in the nominal inversion), and a last inversion assumed that full isostasy is only maintained to degree 60 and transitions to no bottom loads at degree 120. These inversions obtained mare distributions that were consistent with our nominal model with minor (<10%) mare thickness differences (Figure S5). This implies that assumptions on crustal thickness and density, and also in the nature of long-wavelength isostasy are minor when compared to the elastic thickness of the lithosphere. Further discussion on mare thickness and volume for various input crustal structures, together with additional details on the implications of these results for the volcanic inventory of the Moon and mode of emplacement of the maria are given in the companion publication (Broquet & Andrews-Hanna, 2023a).

Our nominal mare thickness estimates within major basins are consistent with earlier work based on flexural modeling and tectonic analyses (~5–10 km, Solomon & Head, 1980), and the mean thickness outside of basins is consistent with previous analyses of buried pre-mare impact craters (~1.5 km, Evans et al., 2016) and geologic investigations of partially buried crater morphology (~1.0–1.5 km, e.g., De Hon 1979). Outside of major basins, the work of Gong et al. (2016) found local mare thickening in western Oceanus Procellarum and near the northwestern edge of the mare region. This local thickening is also obtained in our inversion and is associated with the strong PKT border gravity anomalies (Andrews-Hanna et al., 2014). Interestingly a local thickening of mare basalts in western Oceanus Procellarum is also found from analyses of partially buried craters (De Hon, 1979). However, an alternative scenario has been proposed in which these gravity anomalies could be due to local concentrations of ilmenite-rich cumulates located beneath the crust following magma ocean overturn (Liang et al., 2023a). We note that a combination of both effects is likely. Isostatic compensation of the ilmenite-rich cumulates beneath the crust would lead to an elongated north-south surface depression in western Oceanus Procellarum prior to mare volcanism. Subsequent mare flooding would then locally thicken the maria above the ilmenite bearing cumulates.

Our mare thickness map differs from previous studies that did not explicitly model basin infilling, in which thicknesses of generally less than 3 km (Gong et al., 2016) or 7 km (Williams & Zuber, 1998; Evans et al., 2016) were obtained inside large impact basins. This discrepancy is due to different starting assumptions and to the neglect of lithospheric flexure. The approach in Gong et al. (2016) assumed a statistical correlation between the sub-mare relief and the surface topography. Where mare are thinnest, the surface topography may reflect the sub-mare relief depending on the mare emplacement history. Where the mare are thick, however, and particularly within impact basins, there is no reason that the surface topography should reflect the sub-mare relief located 5 to 10 km below. The spectral analyses of gravity data in the latter work are also limited by a tradeoff between spatial and spectral resolution, resulting in both loss of large areas of the mare and loss of a wide range of degrees. The study of Williams & Zuber (1998) accounted for infilling of basins using a basin depth scaling relationship, but did not account for flexure beneath the mare loads or the variability in basin structure or near/farside

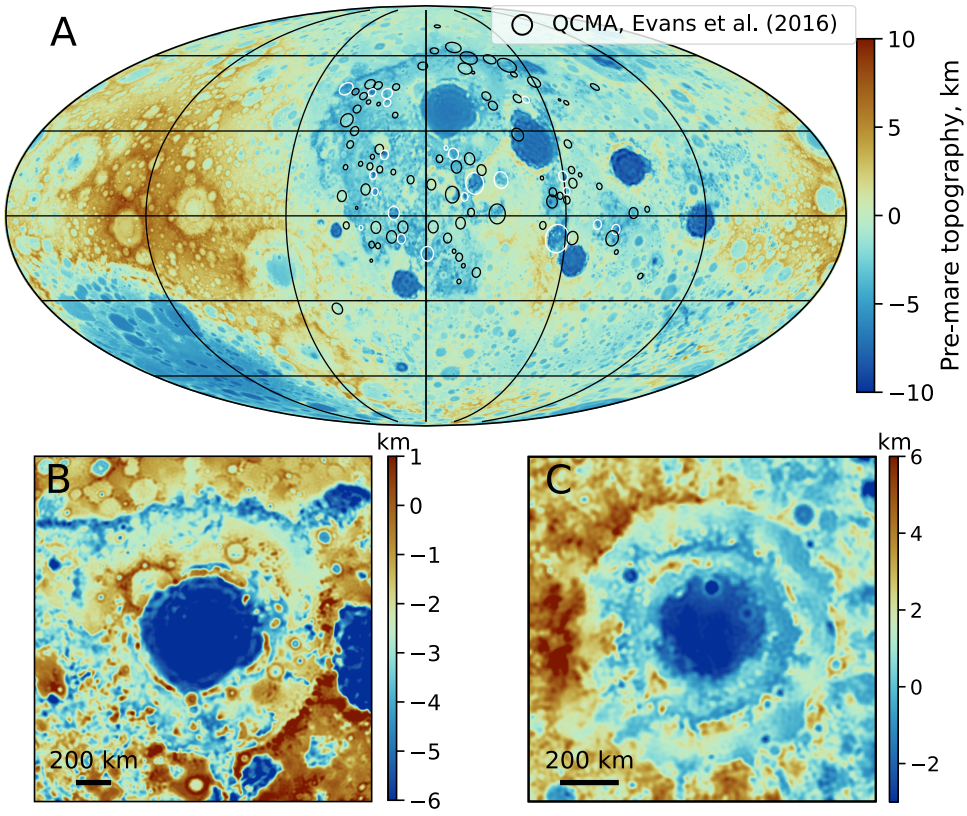

Figure 4: (A) Nominal pre-mare topography superimposed by the quasi-circular mass anomalies (QCMA) of Evans et al. (2016). White circle are those QCMAs we found to be associated with a clear surface depression. (B-C) Zoom in on Imbrium (B) and Orientale (C). Both images are in orthographic projection centered on the basin. A direct comparison between the present-day and pre-mare topography and an unannotated version of the global pre-mare topography map can be found in Figure S7.

differences. The work of Evans et al. (2016) estimated mare thickness based on buried craters observed in gravity data using crater scaling relationships, but this method cannot recover the large mare thicknesses within basins that greatly exceed crater rim heights.

3.3 The pre-mare surface topography

3.3.1. Pre-mare relief of the Procellarum KREEP Terrane

Our inversion also reconstructs the pre-mare topography, which is obtained after having removed from the observed topography the mare deposits and the mare-induced flexure (Figure 4). We note that when computing the pre-mare topography, the removal of the mare load naturally induces a degree-1 shift of the center-of-mass of the pre-mare Moon towards the farside, with an estimated offset of about 850 m. This effect is corrected by removing this degree-1 geoid shift from the pre-mare topography model, resulting in a pre-mare elevation slightly lower than currently observed in the farside (Figure S6). The pre-mare lowlands of the western PKT region stand at about -3 km (1 to 2 km lower than the mare surface elevation) compared to the 4 km elevation of the farside highlands for a total 7 km elevation difference

(Figures S6-S7). The western PKT region is also seen to be 1 to 2 km lower in elevation relative to the surrounding nearside. Although the global lunar topography is characterized by a smooth and continuous degree-1 variation from the farside to the nearside, the distinct change in the pre-mare elevation along the western edge of the mare region suggests the possibility of a discrete change in physical properties there. However, the apparent sharpness of this transition may be accentuated by the superposition of the long-wavelength global asymmetry with the discrete subsurface mass anomalies associated with the PKT border structures which underlie this transition and that have been related to either volcanically flooded rift valleys (Andrews-Hanna et al., 2014) or the gravity signatures of local thickening of a sub-crustal ilmenite-rich layer (Liang et al., 2023a). Nevertheless, the model does support distinctly lower topography within the PKT, which is not the result of the mare-induced deflection given that this quantity has been removed.

There are a few possible explanations for the origin of the western PKT depression. For example, it could be due to the loss of crustal pore space associated with mare-induced pore compaction and thermal annealing linked to a higher regional heat flow throughout the lunar evolution. Following Wieczorek et al. (2013), we assume an initial uniform porosity of 12% throughout a 35 km column of crust, a dry olivine rheology and a constant thermal conductivity of 2.3 W m^{-1} K^{-1}. In that framework, a heat flow increase of 60 mW m^{-2} within the PKT (Laneuville et al., 2013) would cause the depth of viscous pore closure to decrease from below the crust (where we assume no porosity) to 25 km, which could induce 1.2 km of compaction and surface subsidence. For an exponential porosity model with an e-fold depth of 10 to 20 km and surface porosity of 25% (Besserer et al., 2014; Goossens et al., 2022), this would lead to 0.1 to 1.1 km of compaction and subsidence. Alternatively, the isostatic adjustment of a ~150 kg m^{-3} denser nearside crust would be responsible for the 2 km difference in elevation between the surface beneath the maria and the surroundings. Such high crustal densities could be explained by a 6% porosity decrease or equivalent increase in grain density throughout the crustal column with respect to the farside, assuming a bulk crustal density of 2550 kg m^{-3} in the highlands. A higher nearside crustal density may be a result of a more pyroxene-rich crustal composition (Nakamura et al., 2012) or due to intrusive materials beneath the maria of which extent and volume remain unknown (see Broquet & Andrews-Hanna, 2023a). A lower density farside crust has also been suggested based on the relatively low surface concentration of FeO and TiO_2 there (Prettyman et al., 2006; Huang & Wieczorek et al., 2012). If not from density, the elevation difference could be the result of the isostatic compensation of a thinner crust within the PKT region, as assumed in our models as well as previous crustal thickness models. While processes such as asymmetric tidal heating may help explaining the global crustal asymmetry (e.g., Quillen et al., 2019), these would not explain the distinct change at the western edge of the mare region. Finally, having a denser upper mantle beneath the maria, such as due to the presence of ilmenite bearing cumulates following the lunar magma ocean crystallization and overturn (Zhang et al., 2022, Liang et al., 2023a) could also contribute to this elevation difference. A 20 km mantle keel containing dense ilmenite with a density contrast of 350 kg m^{-3} relative to the underlying mantle would result in a ~2 km PKT surface depression with respect to the surrounding highlands.

The idea of a Procellarum impact has been advocated in the literature (e.g., Cadogan et al., 1974; Zhu et al., 2019) and could contribute to both the global crustal asymmetry and the distinctly thinner crust within the PKT. However, the nearside mare-region depression is neither circular nor elliptical in shape and is interrupted by the ancient highland terrains west of Mare Nectaris, making the impact hypothesis difficult to reconcile with the overall morphology of the

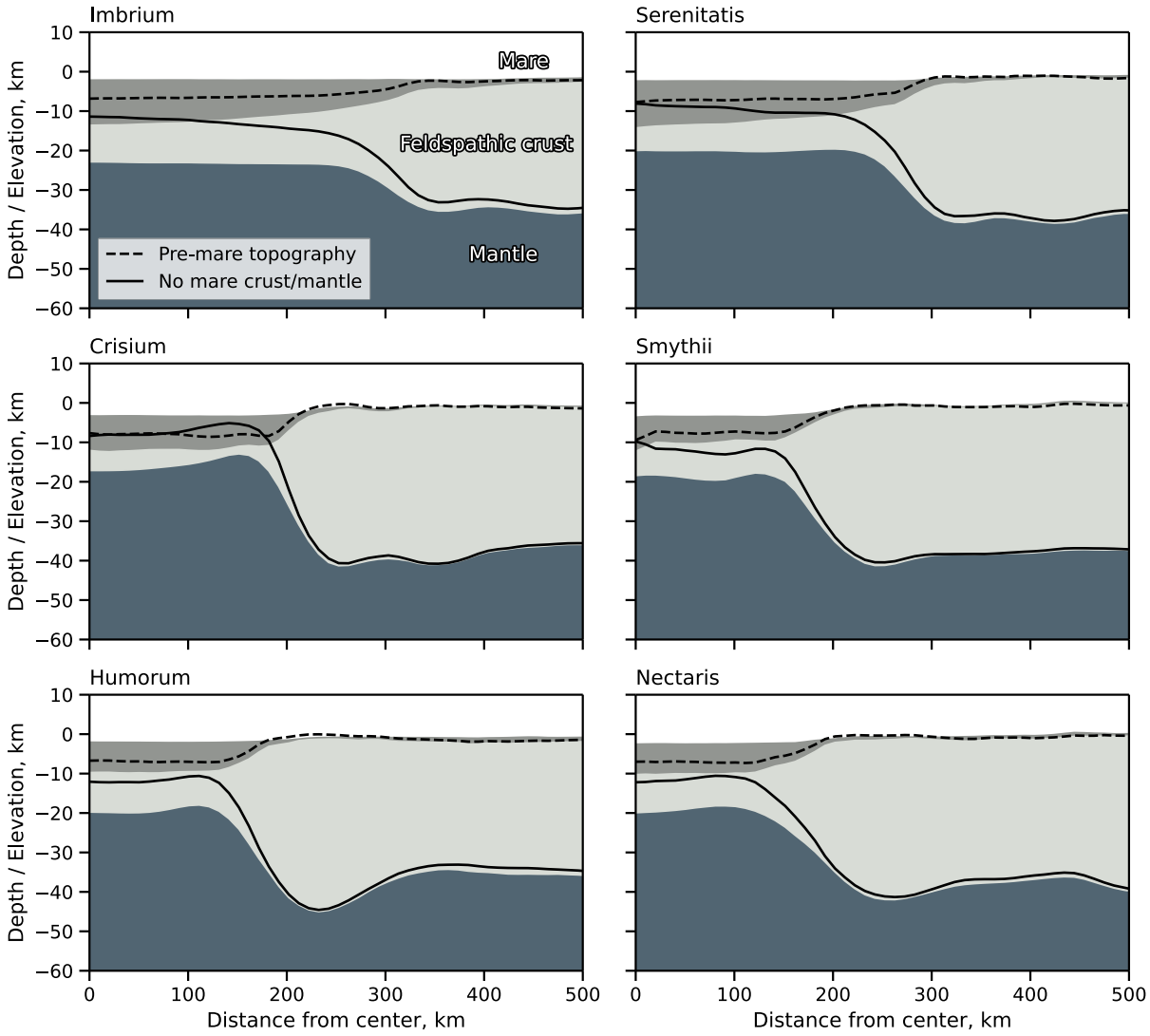

Figure 5: Azimuthally averaged crustal structure for several large mare basins. The dashed line represents the pre-mare topography, and the solid line provides the crust-mantle boundary for a model assuming a 2550 kg m^{-3} constant-density crust.

PKT region (Andrews-Hanna et al., 2014). Finally, the surface depression of the Procellarum region is also reminiscent of that of large igneous provinces as observed on the Earth (e.g., the Columbia River flood basalt province; Reidel et al., 2013), and on Mars (e.g., Hesperia Planum; Broquet & Andrews-Hanna, 2023b). These large igneous provinces sit in depressions of 1 to 2 km with respect to the surroundings with diameters of 800–1700 km, which cannot be explained by the flexural response to surface volcanic loading. An additional source of crustal modification was thus required there beyond the observed volcanism alone. These depressions have been interpreted to be the result of isostatic adjustment following thermal erosion of the crust by the plume that drove flood volcanism (Camp & Hanan, 2008; Broquet & Andrews-Hanna, 2023b). Given the strongly elevated heat flow within the PKT (Laneuville et al., 2013) and complex geodynamic history (e.g., Parmentier et al., 2002; Zhang et al., 2022; Jones et al., 2022), a similar process may have occurred there.

3.3.2. Pre-mare relief of basins and the ring structure of Imbrium

Within the nearside impact basins, the pre-mare (or post-impact) basin floor elevation is predicted to be ~6 km deeper than currently observed due to the presence of thick mare deposits (Figure 4 & 5, see Figure S7 for a direct comparison). For elastic thicknesses of 60 and 20 km, this value ranges from 5 to 7 km, respectively. The pre-mare elevation map also highlights many buried impact craters with diameters of 20 to 200 km, which were previously observed as quasi-circular mass anomalies in Bouguer anomaly maps (Evans et al., 2016) and that appear in our map as actual surface depressions. Some of the buried craters correspond to high relief in the pre-mare topography model, consistent with the interpretation of uplifted feldspathic crust beneath craters embedded within the maria (Evans et al., 2016). However, there is a striking deficit in crater-like depressions at smaller diameters on our modeled pre-mare surface in comparison to the farside highlands, consistent with previous observations (Evans et al., 2018; Liang et al., 2023b). The mid-point of our low-pass taper applied at degrees 350–500 for the mare thickness model corresponds to a half-wavelength of 13 km, indicating that buried craters down to this size should be resolved in the model. The deficit in small buried craters could be due to surface erosion associated with the mare emplacement and flow (Liang et al., 2023b) or other unknown processes.

The pre-mare topography surrounding Imbrium exhibits a marked deviation from present-day elevations, owing to the removal of extensive mare deposits (Figure 4B). That view further highlights the ring structures of Imbrium, which now much more closely resemble the exposed Orientale basin (Figure 4C). A distinct inner ring is exposed locally in the present-day topography as the Montes Pico and Recti. However, the majority of this ring is not visible in observed topography aside from a continuous ring of wrinkle ridges as also found in other mare-filled basins (Byrne et al., 2015). The distinctive ~5 km topographic step of this inner ring in the pre-mare topography results from the removal of the thick mare deposits inside the basin. The inner ring appears to cross the Sinus Iridum crater, which formed after Imbrium. However, this is an artifact of the model assumptions as the relief along the crust-mantle interface at the inner ring affects the pre-mare topography at the relevant range of degrees. The Sinus Iridum crater likely erased the topographic signature of the inner ring, leaving the crust-mantle interface relief intact, while our model partitions the relief between the topography and crust-mantle interface in the isostatic ratio. Imbrium's middle ring, exposed as the Montes Alpes and Archimedes is not expressed differently in the pre-mare topography because of the thin mare layer predicted by the model interior to this ring. However, the outermost ring represented by the Montes Carpatus, Apenninus, and Caucuses is now more clearly expressed. The relief on this ring is increased by the removal of the thick mare deposits interior to these montes, where it is expressed as a 2 to 4 km topographic step.

We emphasize that the pre-mare topography model primarily serves to accentuate the structure of the exposed rings, including clear topographic steps across the inner or outermost ring that were previously embayed by mare on both sides to equal elevations. In contrast, where exposed ring segments do not outcrop above the mare surface, we find no evidence for their existence in the pre-mare topography model. Although discontinuous ring systems can also be observed in Orientale (Figure 4C), the missing ring segments only represent a minor fraction of the exposed ring lengths. For Imbrium, most of the western outer ring structure is missing. Ring formation can be inhibited if the collapse of the transient cavity occurred on a warm lithosphere (Johnson et al., 2016; Bjonnes et al., 2023). However, this would require having an important

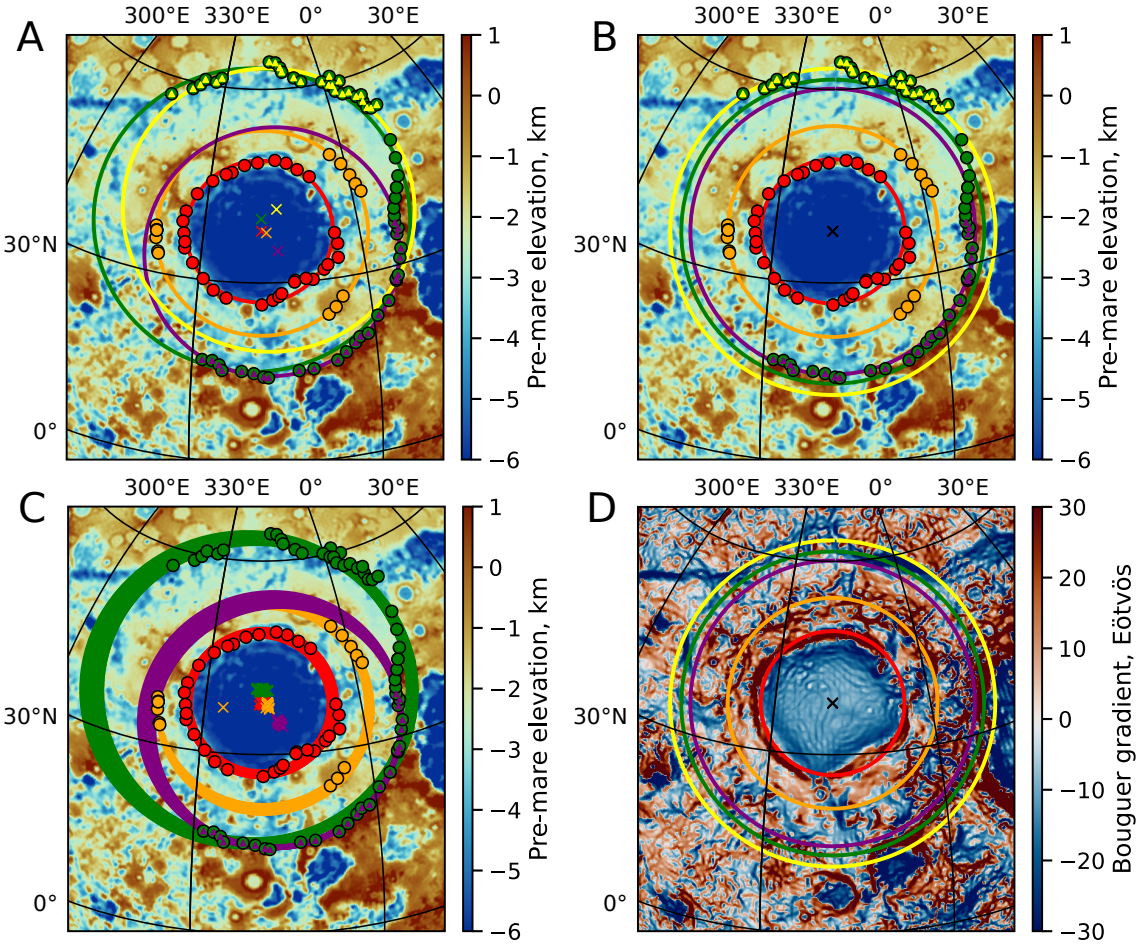

Figure 6: Ring fit at Imbrium. (A) Mapped ring outcrops (colored markers) and simple circular ring fit. (B) Circular ring fit assuming a basin center, as given by the red circle in A. (C) 100 realizations of a bootstrap ring fit. For clarity, the bootstrap fit to the northern part of the ring only is not displayed. (D) Rings shown in B superposed on a Bouguer gradient map. All maps are in orthographic projections centered on Imbrium.

thermal difference between the western and eastern Procellarum region, and this cannot explain the narrow ring gap crossing Mare Frigoris nor the absence of a middle ring south of the basin where the inner and outer rings are well-expressed. Alternatively, the absence of the large western ring segment in both gravity and topography may be related to the missing small crater population beneath the mare, and could involve mare-induced thermo-mechanical erosion (Liang et al., 2023b).

We have mapped the locations where Imbrium's rings outcrop and can be discerned in our pre-mare elevation map (Figure 6). Based on a simple spatial ring fitting method of those points, we find that Imbrium's inner ring is located at an average radial distance of 335 km, with a standard deviation of ±25 km, from a best-fit center located at 341.1°E 37.9°N that is consistent with that found using the middle and outer ring outcrops, within a few degrees. The outer ring of Imbrium has the most complex structure, with the southern part of the ring being ~100 km closer to the basin center than the northern part. For that reason, we also performed a

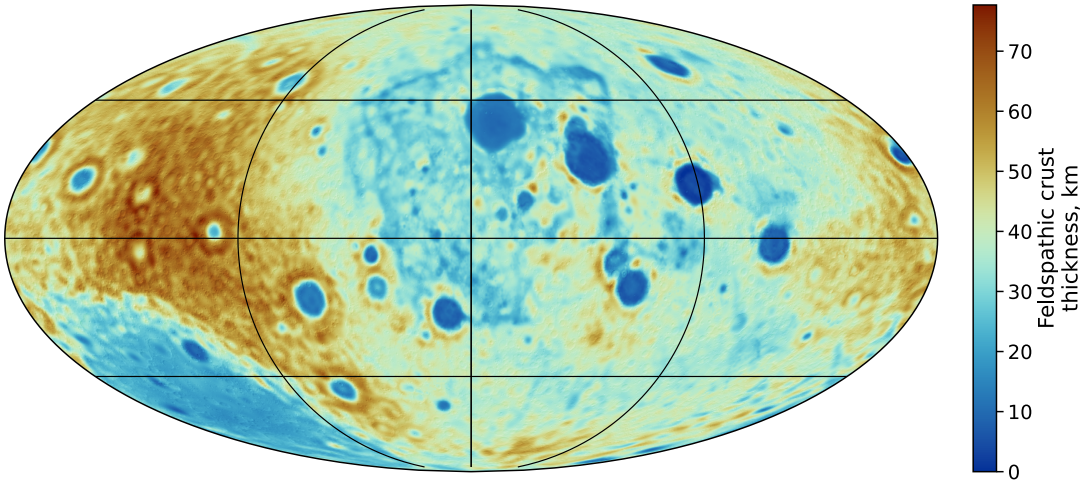

Figure 7: Nominal feldspathic crust thickness map. A direct comparison between the pre-mare and post-mare crust thickness can be found in Figure S7.

ring fit to both the southern and northern part of the outer ring, but found in both cases best-fit center and ring structure inconsistent with the overall basin morphology, implying that those points alone cannot be used to reliably define the outer ring (Figure 6A). In a second approach, we use Imbrium's center as obtained by the better-defined inner ring fit and find that the basin's middle and outer (using all points) rings are located at radial distances of 491±5 and 719±60 km, or at ~1.5 and 2.1 times the inner ring radius (Figure 6B, see also Neumann et al., 2015). Although ring outcrops, apart from the inner ring, are relatively sparse, a simple bootstrapping method applied to our ring fit procedure and based on 100 realizations shows that ring parameters are generally well constrained (Figure 6C). These ring ratios and spacing resemble those of Orientale, with the Outer Rook and Cordillera rings, being located 310 and 462 km (~1.3 and ~2.0 radius) away from the basin center (Andrews-Hanna et al., 2018).

Our outer ring fit is seen to pass close to the Aristarchus plateau to the west near 310°E, particularly when considering the fit to the northern part of Imbrium's ring structure (Figure 6B). This observation is consistent with the interpretation that the plateau was uplifted as part of the outer ring following the Imbrium impact, as suggested in some previous work (Zisk et al., 1977). Interestingly, this further supports the formation of a western ring, and its later erasure by some post-impact processes, such as from mare flood volcanism (Liang et al., 2023b), as the formation of such a short section of a ring in isolation would be unlikely. The ring fit further highlights an offset of the circular outer ring structure of Imbrium to the east and north, where the outer ring is located further away from the basin center than observed elsewhere (Figure 6B). This offset begins in the middle of the Montes Caucuses, and aligns with the northern edge of central Mare Frigoris, interrupted by a narrow gap in the mare itself. This implies that some level of crustal or lithospheric variability may have affected ring formation at the time of impact. Interestingly, the northernmost segment of the outer ring lies just beyond the prominent negative gravity gradient anomalies that surround the PKT region. The gravity anomalies have been argued to be due to local density anomalies at depth, potentially linked to mare-flooded ancient rift zones, the magma plumbing system of the maria (Figure 6D; Andrews-Hanna et al., 2014), or to local

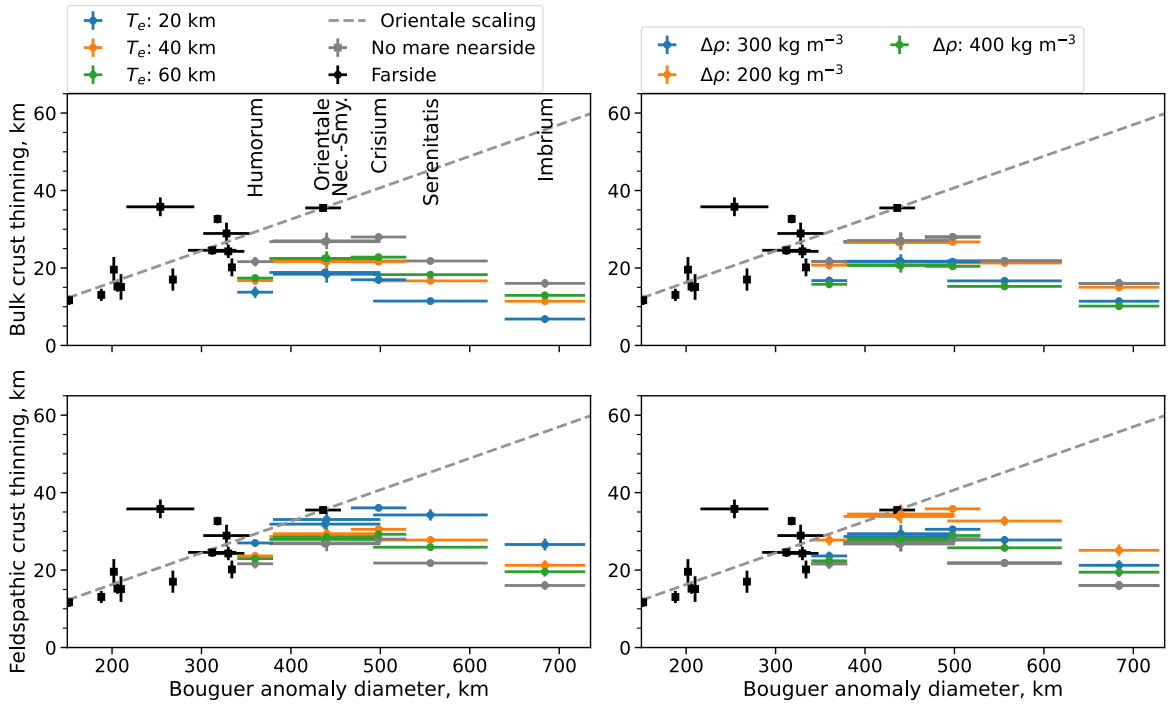

Figure 8: Thinning of the bulk (feldspathic + mare) (A-B) and feldspathic crust (C-D) within large basins as a function of their average Bouguer anomaly diameter (Neumann et al., 2015), for various elastic thickness (T_e) and density contrast between the mare and feldspathic crust ($\Delta\rho$). The horizontal bar denotes the uncertainty in the Bouguer diameter, and the vertical bar denotes the standard deviation. The dashed line indicates a crustal thinning extrapolation based on Orientale. Farside basins not annotated include (from left to right) Copernicus, Poincaré, Korolev, Lamont, Fowler-Charlier, Hertzsprung, Crüger-Sirsalis, Humboldtianum, Freundlich-Sharonov, Mendel-Rydberg, Coulomb-Sarton, and Fitzgerald-Jackson.

remnants of ilmenite bearing cumulates in the upper mantle (Liang et al., 2023a). Thus, it is possible that this lithospheric variability contributed to the outward shift of this ring segment.

3.4 Crustal structure of nearside impact basins

The feldspathic crust within large impact basins is ~7 km thinner in comparison to models with a constant density crust (Figure 5 and 8C-D; Figures S7 and S8). For elastic thicknesses of 60 and 20 km, this value ranges from 5 to 12 km, respectively. In all simulations, the minimum crustal thickness is obtained within Mare Crisium where it approaches a value of zero, implying that the impact event excavated through the crust, which consistent with surface exposures of olivine in the vicinity of the basin (Yamamoto et al., 2010). Together, these may have important implications for the characterization of the impact process (Freed et al., 2001; Melosh et al., 2013) and crustal temperature (Miljković et al., 2016; Ding & Zhu, 2022).

Differences in the feldspathic (pre-mare) crustal structure between the nearside and farside basins can also help reveal variations in the thermo-mechanical properties and composition of the lithosphere. The crustal thinning beneath several large basins was estimated from the difference between an azimuthal average far from (1.8× crater radius away) and within

(<100 km) the basin center for various elastic thicknesses at the time of mare emplacement (20–60 km) and density structures (200–400 kg m^{-3} density difference between mare and crust; Figure 8). Both stronger lithospheres and higher density contrasts between the mare and crust decrease the amount of thinning predicted by our inversion. The maximum amount of thinning is obtained for a basin diameter of ~450–500 km (Orientale, Nectaris, Smythii, Crisium), with both smaller and larger basins exhibiting less thinning. At the large end, this is likely due to those basins having excavated through the whole crust, as evident from surface exposures of olivine around many basins (Yamamoto et al., 2010), combined with the generation of new crust from the impact melt ponds (Hawke & Head, 1977; Hurwitz & Kring 2014) and the flow of crust from outside the excavated zone across the basin center (Melosh et al. 2013, Freed et al., 2014, Johnson et al., 2016). Humorum, Smythii, and Nectaris are seen to have relatively consistent, though slightly less, crustal thinning than an appropriately scaled Orientale. In all cases, smaller density contrasts and thinner lithospheres at the time of mare volcanism allow the nearside basins to approach our Orientale scaling more closely, which is consistent with our tectonic analysis also favoring thin lithospheres in these basins. Nevertheless, the relatively reduced crustal thinning on the nearside could also be linked to the warmer crust of the PKT region, as impacts on hot targets generally lead to greater basin diameters and less crustal thinning, both because of the collapse of the transient crater cavity (e.g., Miljković et al., 2016).

The crustal thinning variation further suggests that the Imbrium- and Serenitatis-forming impacts excavated substantially below the crust, about 20–40 and 10–20 km, respectively. Given that the amount of crust and mantle excavated by the Imbrium impact are roughly equivalent in volume, the KREEP signature in Imbrium's ejecta (Haskin et al., 1998) could either be of crustal or mantle origin. In contrast, the overall lack of KREEP signature in Serenitatis' ejecta cannot be due to the basin not excavating deeply enough, and is likely due to the crust and mantle being initially KREEP-poor.

4. Conclusion

In this work, we inverted gravity and topography data for the structure of the crust and mare matching the expectation for an approximately long-wavelength isostatic pre-mare crust. Using constraints from the tectonic record and partially buried crater population, the bulk of mare emplacement was constrained to have occurred on a 40-km-thick elastic lithosphere, which is consistent with previous estimates (e.g., Solomon & Head, 1980) and thermal evolution models (Laneuville et al., 2013). Mare within large basins may have formed on thinner lithospheres (~20 km), but more work is required regarding the influence on basin tectonics of the loading by the crustal annulus and post-impact intrusive magmatism, and of zones of weakness related to the impact event.

Mare thicknesses are found to significantly vary across the nearside being principally concentrated within large impact basins with an average thickness of about 8 km, significantly higher than the average outside these basins of 1.6 km. A strong tradeoff between mare thickness and the elastic thickness of the lithosphere at the time of mare emplacement was observed. For example, for elastic thicknesses of 20 to 60 km, the mean mare thickness within nearside basins ranges from about 6 to 15 km. While our average mare thickness outside major basins is consistent with previous studies (e.g., De Hon, 1979; Evans et al., 2016), our work potentially finds volumes of mare twice as large (~2.0×10^7 km^3) than typically estimated from the mare thickness outside major basins (Head & Wilson, 1992). This important difference is due to our

model accounting for mare-induced flexure that leads to large mare deposits within major nearside basins. Our global and continuous mare inversion sheds light on the overall concentration of mare materials within large basins, with important implications for our understanding of the mode of emplacement of mare volcanism, the dynamics of magma ascent, and the volumetric ratio of intrusive:extrusive activity, as further discussed in Broquet & Andrews-Hanna (2023a).

We reconstructed the topography of the Moon before mare volcanism. The western PKT region is ~2 km than the surrounding nearside, and large nearside basins are 6 km deeper than currently observed. Both are useful quantities for studies addressing the primordial structure of the Moon before mare volcanism obscured the surface and crust. For example, the overall depression of the Procellarum region cannot be explained by mare volcanism alone, and requires an additional source of crustal modifications, with possible explanations involving isostatic adjustment of a denser or thinner nearside crust, thermal compaction, large-scale crustal intrusions, the presence of ilmenite-rich cumulates below the crust, or crustal erosion induced by a mantle plume or thermal anomaly. The pre-mare topography further highlights the ring structure around Imbrium. Based on a ring fit algorithm, the relative distances to the inner, middle, and outer rings are found to be consistent with those of the Orientale basin. We observed an offset of the outer ring to the east and north, which could be related to lateral variations in the thermal or mechanical properties of the lithosphere at the time of impact and ring formation. One source of variability could be linked to the borders of the PKT region that are associated with strong gravity gradient anomalies potentially linked to mare-flooded ancient rift zones and the magma plumbing system of the maria (Andrews-Hanna et al., 2013), or the presence of ilmenite bearing cumulates below the crust (Liang et al., 2023a). Our pre-mare topography does not show evidence for the rings where buried beneath the maria, including a western Imbrium ring or any segments of either the middle or outer ring. This implies either that these ring segments never formed or were erased following the basin formation. The latter explanation could be related to the missing small crater population on the nearside suggested to be a result of mare-induced thermo-mechanical erosion (Evans et al., 2018; Liang et al., 2023b).

By accounting for the density difference between the mare and underlying feldspathic crust, we present a more accurate crustal thickness model of the Moon. Our nominal models with an elastic thickness of 40 km at the time of mare emplacement obtain feldspathic crustal thicknesses that are ~7 km thinner within large basins than in constant crustal density models (e.g., Wieczorek et al., 2013), and up to 12 km thinner for an elastic thickness of 20 km. When considering the bulk crust (feldspathic + mare), our nominal crustal thicknesses beneath the maria are ~5 km thicker than in models assuming a constant crustal density. These updated crustal thickness maps further reveal that crustal thinning following large impacts is more drastic in the nearside than previously thought, with implications for simulations of basin formation and evolution (Melosh et al., 2013; Freed et al., 2014). Together, these results demonstrate that mare materials must be accounted for when investigating the internal structure of the large nearside basins and the Moon as a whole.

Data availability:

All data and code are public and accessible on GitHub or the PDS, as noted in the Acknowledgments.

Acknowledgments:

The data used in this study can be found on the NASA PDS Geosciences website (https://pds-geosciences.wustl.edu/). The nominal, mare, feldspathic crust, bulk crust, and pre-mare elevation models can be found at 10.5281/zenodo.8348278. The thin-shell flexural model can be found at Broquet (2022a), the elastic thickness to heat flow code can be found at Broquet (2022b), and some of this work made use of the SHTOOLS package of Wieczorek & Meschede (2018). We thank 2 anonymous reviewers for their thoughtful comments that helped improve this manuscript. This work was supported by grant 80NSSC22K1340 from the NASA Lunar Data Analysis Program to JCAH.

References

Andrews-Hanna, J. C., (2013), The origin of the non-mare mascon gravity anomalies in lunar basins. *Icarus* **222**, 159–168. doi:10.1016/j.icarus.2012.10.031.

Andrews-Hanna, J. C., Besserer, J., Head, J. W., et al. (2014), Structure and evolution of the lunar Procellarum region as revealed by GRAIL gravity data. *Nature* **514**, 68–71. doi:10.1038/nature13697.

Andrews-Hanna, J. C., Head, J. W., Johnson, B., et al. (2018), Ring faults and ring dikes around the Orientale basin on the Moon. *Icarus* **310**, 1–20. doi:10.1016/j.icarus.2017.12.012.

Banerdt, W. B. (1986), Support of long-wavelength loads on Venus and implications for internal structure. *J. Geophys. Res.* **91(B1)**, 403–419. doi:10.1029/JB091iB01p00403.

Besserer, J., Nimmo, F., Wieczorek, M. A., et al. (2014), GRAIL gravity constraints on the vertical and lateral density structure of the lunar crust, *Geophys. Res. Lett.* **41**, 5771–5777. doi:10.1002/2014GL060240.

Bjonnes, E., Johnson, B. C., & Andrews-Hanna, J. C. (2023), Basin Crustal Structure at the Multiring Basin Transition. *J. Geophys. Res. Planets* **128**, e2022JE007507. doi:10.1029/2022JE007507.

Broquet, A., (2022a), AB-Ares/Displacement_strain_planet : Version 0.4.0. Zenodo. doi:10.5281/zenodo.7196507.

Broquet, A., (2022b), AB-Ares/Te_HF_Conversion: Version 0.2.3. Zenodo. doi:10.5281/zenodo.4973893

Broquet, A., & Andrews-Hanna, J. C. (2022), Geophysical evidence for an active mantle plume underneath Elysium Planitia on Mars. *Nat. Astro*. doi:10.1038/s41550-022-01836-3.

Broquet, A., & Andrews-Hanna, J. C. (2023a), Volcanic inventory on the Moon, *in prep*.

Broquet, A., & Andrews-Hanna, J. C. (2023b), Plume-induced flood basalts on Hesperian Mars: An investigation of Hesperia Planum. *Icarus* **391**, 115338. doi:10.1016/j.icarus.2022.115338.

Byrne, P. K., Klimczak, C., McGovern, P. J., et al., (2015), Deep-seated thrust faults bound the Mare Crisium lunar mascon. *Earth Planet. Sci. Lett.* **427**, 183–190. doi:10.1016/j.epsl.2015.06.022.

Cadogan, P. H. (1974), Oldest and largest lunar basin? *Nature* **250**, 315–316. doi:10.1038/250315a0.

Callihan, M. B., & Klimczak, C. (2019), Topographic expressions of lunar graben. *Lithosphere* **11(2)**, 294–305. doi:10.1130/L1025.1.

Camp, V. E., & Hanan, B. B. (2008), A plume-triggered delamination origin for the Columbia River Basalt Group. *Geosphere* **4(3)**, 480–495. doi:10.1130/GES00175.1.

Crameri, F. (2018), Scientific colour maps: perceptually uniform and colour-vision deficiency friendly. Zenodo. doi:10.5281/zenodo.1243862.

Dahlen, F. A. (1982), Isostatic geoid anomalies on a sphere, *J. Geophys. Res.* **87(B5)**, 3943–3947. doi:10.1029/JB087iB05p03943.

De Hon, R. A. (1974), Thickness of mare material in the Tranquillitatis and Nectaris basins. *5th Lunar and Planetary Science Conference* **1**, 53–59.

De Hon, R. A. (1979), Thickness of the western mare basalt. *10th Lunar and Planetary Science Conference* **3**, 2935–2955.

De Hon, R. A., & Waskom, J. D. (1976), Geologic structure of the eastern mare basins. *7th Lunar and Planetary Science Conference* **3**, 2729–2746.

Ding, M., & Zhu, M.-H. (2022), Effects of regional thermal state on the crustal annulus relaxation of lunar large impact basins. *J. Geophys. Res. Planets* **127**, e2021JE007132. doi:10.1029/2021JE007132.

Du, J., Fa, W., Wieczorek, M. A., et al. (2019), Thickness of lunar mare basalts: New results based on modeling the degradation of partially buried craters. *J. Geophys. Res. Planets* **124**, 2430–2459. doi:10.1029/2018JE005872.

Evans, A. J., Andrews-Hanna, J. C., Head, J. W., et al. (2018), Reexamination of early lunar chronology with GRAIL data: Terranes, basins, and impact fluxes. *J. Geophys. Res. Planets* **123**, 1596– 1617. doi:10.1029/2017JE005421.

Evans, A. J., Soderblom, J. M., Andrews-Hanna, J. C., et al. (2016), Identification of buried lunar impact craters from GRAIL data and implications for the nearside maria. *Geophys. Res. Lett.* **43**, 2445–2455. doi:10.1002/2015GL067394.

Fortezzo, C. M., Spudis, P. D. & Harrel, S. L. (2020), Release of the Digital Unified Global Geologic Map of the Moon At 1:5,000,000- Scale. *51st Lunar and Planetary Science Conference* **2760**.

Freed, A. M., Johnson, B. C., Blair, D. M., et al. (2014), The formation of lunar mascon basins from impact to contemporary form. *J. Geophys. Res. Planets* **119**, 2378–2397. doi:10.1002/2014JE004657.

Freed, A. M., Melosh, H. J., & Solomon, S. C. (2001), Tectonics of mascon loading: Resolution of the strike-slip faulting paradox. *J. Geophys. Res.* **106(E9)**, 20603–20620. doi:10.1029/2000JE001347.

Garrick-Bethell, I., Nimmo, F., & Wieczorek, M. A. (2010), Structure and formation of the lunar farside highlands. *Science* **330**, 949–951. doi:10.1126/science.1193424.

Gong, S., Wieczorek, M. A., Nimmo, F., et al. (2016), Thicknesses of mare basalts on the Moon from gravity and topography. *J. Geophys. Res. Planets* **121**, 854–870. doi:10.1002/2016JE005008.

Goossens, S., Sabaka, T. J., Wieczorek, M. A., et al. (2020), High-resolution gravity field models from GRAIL data and implications for models of the density structure of the Moon's crust. *J. Geophys. Res. Planets* **125**, e2019JE006086. doi:10.1029/2019JE006086.

Haskin, L. A. (1998), The Imbrium impact event and the thorium distribution at the lunar highlands surface, *J. Geophys. Res.* **103(E1)**, 1679–1689. doi:10.1029/97JE03035.

Hawke, B. R., & Head, J. W. (1977), Impact melt in lunar crater interiors. D.J. Roddy, R.O. Pepin, R.B. Merrill (Eds.), Impact and Explosion Cratering, Pergamon Press, New York, NY, p. 815.

Head, J. W. (1982), Lava flooding of ancient planetary crusts: Geometry, thickness, and volumes of flooded lunar impact basins. *The Moon and the Planets* **26**, 61–88. doi:10.1007/BF00941369.

Head, J. W., & Wilson, L. (1992), Lunar mare volcanism: Stratigraphy, eruption conditions, and the evolution of secondary crusts. *Geochim. Cosmochim. Acta* **56**, 2155–2175. doi:10.1016/0016-7037(92)90183-J.

Head, J. W., & Wilson, L. (2017), Generation, ascent and eruption of magma on the Moon: New insights into source depths, magma supply, intrusions and effusive/explosive eruptions (Part 2: Observations). *Icarus* **283**, 176–223. doi:10.1016/j.icarus.2016.05.031.

Hemingway, D. J., & Matsuyama, I. (2017), Isostatic equilibrium in spherical coordinates and implications for crustal thickness on the Moon, Mars, Enceladus, and elsewhere, *Geophys. Res. Lett.* **44**, 7695– 7705. doi:10.1002/2017GL073334.

Hiesinger, H., Head, J. W., Wolf, U., et al. (2011), Ages and stratigraphy of lunar mare basalts: A synthesis. *Geol. Soc. Am. Spec.* **477**, 1–51. doi:10.1130/2011.2477(01).

Huang, Q., & Wieczorek, M. A. (2012) Density and porosity of the lunar crust from gravity and topography. *J. Geophys. Res.* **117**, (E5), E05003. doi:10.1029/2012JE004062.

Hurwitz, D. M., & Kring, D. A. (2014), Differentiation of the South Pole–Aitken basin impact melt sheet: Implications for lunar exploration, *J. Geophys. Res. Planets* **119**, 1110–1133. doi:10.1002/2013JE004530.

Johnson, B. C., Blair, D. M., Collins, G. S., et al. (2016), Formation of the Orientale lunar multiring basin. *Science* **354(6311)**, 441–444. doi:10.1126/science.aag0518.

Jones, M. J., Evans, J. A., Johnson, B. C, et al. (2022), A South Pole–Aitken impact origin of the lunar compositional asymmetry. *Sci. Adv.* **8**, eabm8475. doi:10.1126/sciadv.abm8475.

Kiefer, W. S., Macke, R. J., Britt, D. T., et al. (2012), The density and porosity of lunar rocks, *Geophys. Res. Lett.* **39**, L07201. doi:10.1029/2012GL051319.

Klimczak, C. (2014), Geomorphology of lunar grabens requires igneous dikes at depth. *Geology* **42(11)**, 963–966. doi:10.1130/G35984.1.

Konopliv, A. S., Park, R. S., Yuan, D.-N., et al. (2014), High-resolution lunar gravity fields from the GRAIL Primary and Extended Missions. *Geophys. Res. Lett.* **41**, 1452–1458. doi:10.1002/2013GL059066.

Laneuville, M., Wieczorek, M. A., Breuer, D., et al. (2013), Asymmetric thermal evolution of the Moon. *J. Geophys. Res. Planets* **118**, 1435–1452. doi:10.1002/jgre.20103.

Liang, W., Andrews-Hanna, J. C., & Evans, A. J., (2023b), The missing craters and basin rings beneath the lunar maria, *submitted to JGR-Planets.*

Liang, W., Broquet, A., Andrews-Hanna, J. C., et al. (2023a), Vestiges of a lunar ilmenite layer revealed by GRAIL gravity data. *submitted to Nat. Geosci.*

Matsuyama, I., Trinh, A., & Keane, J. T. (2021), The Lunar Fossil Figure in a Cassini State. *Planet. Sci.* **2(232)**. doi:10.3847/PSJ/ac32d9.

Melosh, H. J., Freed, A. M., Brandon C. J., et al. (2013), The origin of lunar mascon basins. *Science* **340**, 1552–1555. doi:10.1126/science.1235768.

Miljković, K., Collins, G. S., Wieczorek, M. A., et al. (2016), Subsurface morphology and scaling of lunar impact basins. *J. Geophys. Res. Planets* **121**, 1695–1712. doi:10.1002/2016JE005038.

Mohit, P. S., and Phillips, R. J. (2006), Viscoelastic evolution of lunar multiring basins, *J. Geophys. Res.* **111**, E12001. doi:10.1029/2005JE002654.

Nakamura, R., Yamamoto, S., Matsunaga, T. et al. (2012), Compositional evidence for an impact origin of the Moon's Procellarum basin. *Nat. Geosci.* **5**, 775–778. doi:10.1038/ngeo1614.

Nelson, D. M., Koeber, S. D., Daud, K., et al. (2014), Mapping lunar maria extents and lobate scarps using LROC image products. *45th Lunar and Planetary Science Conference*.

Parmentier, E. M., Zhong, S., & Zuber, M. T. (2002), Gravitational differentiation due to initial chemical stratification: origin of lunar asymmetry by the creep of dense KREEP? *Earth Planet. Sci. Lett.* **201**, 473–480. doi:10.1016/S0012-821X(02)00726-4.

Pasckert, J. H., Hiesinger, H., & van der Bogert, C. H. (2018), Lunar farside volcanism in and around the South Pole–Aitken basin. *Icarus* **299**, 538–562. doi:10.1016/j.icarus.2017.07.023.

Prettyman, T. H., Hagerty, J. J., Elphic, R. C., et al. (2006), Elemental composition of the lunar surface: Analysis of gamma ray spectroscopy data from Lunar Prospector, *J. Geophys. Res.* **111**, E12007. doi:10.1029/2005JE002656.

Quillen, A. C., Martini, L., & Nakajima, M. (2019), Near/far side asymmetry in the tidally heated Moon. *Icarus* **329**, 182–196. doi:10.1016/j.icarus.2019.04.010.

Reidel, S. P., Camp, V. E., Tolan, T. L., et al. (2013), Tectonic evolution of the Columbia River flood basalt province. In: The Columbia River Flood Basalt Province. Geological Society of America. doi:10.1130/2013.2497(12).

Ritzer, J. A., & Hauck, S. A. (2009), Lithospheric structure and tectonics at Isidis Planitia, Mars, *Icarus* **201**, 528–539. doi:10.1016/j.icarus.2009.01.025.

Searls, M. L., Banerdt, W. B., & Phillips, R. J. (2006), Utopia and Hellas basins, Mars: Twins separated at birth, *J. Geophys. Res.* **111**, E08005. doi:10.1029/2005JE002666.

Shearer, C., Hess, P. C., Wieczorek, M. A., et al. (2006), Thermal and magmatic evolution of the Moon, *Rev. Mineral. Geochem.* **60**, 365–518. doi:10.2138/rmg.2006.60.4.

Smith, D. E., Zuber, M. T., Neumann, A., et al. (2010), Initial observations from the Lunar Orbiter Laser Altimeter (LOLA). *Geophys. Res. Lett.* **37**, L18204. doi:10.1029/2010GL043751.

Solomon, S. C., & Head, J. W. (1980), Lunar mascon basins: Lava filling, tectonics, and evolution of the lithosphere. *Rev. Geophys.* **18(1)**, 107–141. doi:10.1029/RG018i001p00107.

Sori, M. M., Zuber, M. T., Head, J. W., et al. (2016), Gravitational search for cryptovolcanism on the Moon: Evidence for large volumes of early igneous activity. *Icarus* **273**, 284–295. doi:10.1016/j.icarus.2016.02.009.

Thomson, B. J., Grosfils, E. B., Bussey, D. B. J., et al. (2009), A new technique for estimating the thickness of mare basalts in Imbrium Basin. *Geophys. Res. Lett.* **36**, L12201. doi:10.1029/2009GL037600.

Vaucher, J., Baratoux, D., Mangold, N., et al. (2009), The volcanic history of central Elysium Planitia: implications for Martian magmatism. *Icarus* **204**, 418–442. doi:10.1016/j.icarus.2009.06.032.

Watters, T. R., & Johnson, C. L., (2010), Lunar tectonics, in Watters, T.R., & Schultz, R.A., eds., Planetary Tectonics : New York, Cambridge University Press, 121–182.

Whitten, J. L., & Head, J. W. (2015), Lunar cryptomaria: Physical characteristics, distribution, and implications for ancient volcanism. *Icarus* **247**, 150–171. doi:10.1016/j.icarus.2014.09.031.

Whitten, J., Head, J. W., Staid, M., et al. (2011), Lunar mare deposits associated with the Orientale impact basin: New insights into mineralogy, history, mode of emplacement, and relation to Orientale Basin evolution from Moon Mineralogy Mapper (M3) data from Chandrayaan-1. *J. Geophys. Res. Planets* **116**, E00G09. doi:10.1029/2010JE003736.

Wieczorek, M. A., & Meschede, M., (2018), Shtools: tools for working with spherical harmonics. *Geochem. Geophys. Geosyst.* **19**, 2574–2592. doi:10.1029/ 2018GC007529.

Wieczorek, M. A., & Phillips, R. J. (1999), Lunar Multiring Basins and the Cratering Process. *Icarus*, **139**, 246–259. doi:10.1006/icar.1999.6102.

Wieczorek, M. A., Neumann, G. A., Nimmo, F., et al. (2013), The crust of the Moon as seen by GRAIL. *Science* **339(6120)**, 671–675. doi:10.1126/science.1231530.

Williams, K. K., & Zuber, M. T. (1998), Measurement and Analysis of Lunar Basin Depths from Clementine Altimetry. *Icarus* **131**, 107–122. doi:10.1006/icar.1997.5856.

Wilson, L., & Head, J. W. (2017), Generation, ascent and eruption of magma on the Moon: New insights into source depths, magma supply, intrusions and effusive/explosive eruptions (Part 1: Theory). *Icarus* **283**, 146–175. doi:10.1016/j.icarus.2015.12.039.

Wood, J. A., Dickey, J. S., Marvin, U. B., et al. (1970), Lunar anorthosites. *Science* **167(3918)**, 602–604. doi:10.1126/science.167.3918.602.

Yamamoto, S., Nakamura, R., Matsunaga, T., et al. (2010), Possible mantle origin of olivine around lunar impact basins detected by SELENE. *Nat. Geosci.* **3**, 533–536. doi:10.1038/ngeo897.

Zhang, N., Ding, M., Zhu, M. H., et al. (2022), Lunar compositional asymmetry explained by mantle overturn following the South Pole–Aitken impact. *Nat. Geosci.* **15**, 37–41. doi:10.1038/s41561-021-00872-4.

Zhu, M.-H., Wünnemann, K., Potter, R. W. K., et al. (2019), Are the Moon's nearside-farside asymmetries the result of a giant impact? *J. Geophys. Res. Planets* **124**, 2117–2140. doi:10.1029/2018JE005826.

Appendix A: Key equations for our global mare thickness inversion

The thin-shell loading model used in this work is defined in spherical harmonics, with *l* and *m* being the spherical harmonic degree and order respectively (see Banerdt et al., 1986; Broquet, 2022a; Broquet & Andrews-Hanna, 2022, 2023b). Compared to the formulation presented in our previous work, the model has here been updated to include an additional interface associated with the mare load. Below, we provide the key equations that define this updated model.

The first equation describes the total net load on the lithosphere and relates the surface topography (H_{lm}), the observed geoid (G_{lm}), flexure (w_{lm}), the top (tc_{lm}) and bottom (bc_{lm}) loads in the feldspathic crust, and the geoid at the base of the crust (Gc_{lm}) as

$$q_{lm} = g_0\rho_{mare}(H_{lm} - G_{lm}) + g_m\Delta\rho_1(w_{lm} - bc_{lm} - Gc_{lm}) + g_0\Delta\rho_2(w_{lm} - tc_{lm} - G_{lm}). \quad \text{(A1)}$$

In this equation $\Delta\rho_1 = (\rho_m - \rho_c)$, $\Delta\rho_2 = (\rho_c - \rho_{mare})$; ρ_m, ρ_c, and ρ_{mare} are the density of the mantle, feldspathic crust, and mare basalts; g_0 and g_m are the vertical gravitational acceleration at the surface and crust-mantle boundary. Note that the gravitational attraction at the mare-crust interface, which is located 1.9 km below the surface in our nominal model, is assumed to be the same than at the surface. In our model, the global mare thickness is defined as $H_{lm} - (w_{lm} - tc_{lm})$.

The second equation links the top and bottom loads in the feldspathic (pre-mare) crust assuming an equal pressure isostatic balance

$$g_m(\rho_m - \rho_c)bc_{lm} + g_0\rho_c tc_{lm}\gamma = 0, \quad \text{(A2)}$$

in which γ is the isostatic correction factor that is varied from 0.9 to 1.1 (Figure S5).

In the case where density anomalies are considered as mass-sheets, the geoid at the surface associated with the contribution of all interfaces can be derived as

$$G_{lm} = \frac{3}{\bar{\rho}(2l+1)}\{\rho_c H_{lm} + \Delta\rho_1(w_{lm} - bc_{lm})\varphi^{l+2} + \Delta\rho_2(w_{lm} - tc_{lm})\psi^{l+2}\} \quad \text{(A3)}$$

where, $\varphi = (R - T_c)/R$; $\psi = (R - T_m)/R$; T_m is the reference height of the pre-mare surface (1.9 km in our nominal model), R and $\bar{\rho}$ are the mean planetary radius and density, respectively, and T_c is the average crustal thickness. Similarly, the geoid at the base of the crust is given by

$$Gc_{lm} = \frac{3g_0}{\bar{\rho}(2l+1)g_m}\left\{\rho_c H_{lm}\varphi^l + \Delta\rho_1(w_{lm} - bc_{lm})\varphi + \Delta\rho_2(w_{lm} - tc_{lm})\frac{\varphi^{l+1}}{\psi^{l+1}}\psi\right\}. \quad \text{(A4)}$$

Finally, the tangential load potential can be expressed as

$$\begin{aligned}\Omega_{lm} = \frac{v}{1-v}\Big[&\rho_{mare}g_0T_e\frac{H_{lm}}{R} + \Delta\rho_1 g_m(T_e - T_m - T_c)\frac{bc_{lm}}{R} + \Delta\rho_2 g_0(T_e - M)\frac{tc_{lm}}{R} \\ &- \Delta\rho_2 g_0(T_e - M)\frac{w_{lm}}{R}\Big] \\ &+ [\rho_{mare}g_0T_m + \rho_c g_m T_c + \rho_m g_m(T_e - T_m - T_c)]\frac{w_{lm}}{R} \quad \text{(A5)}\end{aligned}$$

where v is Poisson's ratio assumed to be equal to 0.25, T_e is the elastic thickness of the lithosphere. Our equation for lithospheric flexure is identical to equation A5 in Broquet & Andrews-Hanna (2022), and the strain tensor definition can be found in equations A12–A21 in Banerdt et al., (1986).

Appendix B: Correction to the lunar fossil figure

In Garrick-Bethell et al. (2010), the degree-2 uncompensated ($H_{2,m,u}$) and compensated ($H_{2,m,c}$) topography coefficients were linked to observed basin-corrected gravity ($C_{2,m}$) and topography ($T_{2,m}$) as

$$H_{2,m,c} = \frac{A_1C_{2,m} - T_{2,m}}{A_2A_3 - 1} \;\; ; \;\; H_{2,m,u} = \frac{A_1C_{2,m} - T_{2,m}A_2A_3}{1 - A_2A_3}$$

where

$$A_1 = \frac{5\bar{\rho}R}{3\rho_c}; \;\; A_2 = 1 + \frac{\rho_c}{(\rho_m - \rho_c)}; \;\; A_3 = \frac{4c(\rho_m - \rho_c)}{R\rho_m}$$

in which ρ_m, ρ_c, $\bar{\rho}$, R, and c are the crust, mantle, and mean lunar density, and the mean planetary radius and crustal thickness. In the system, $A_1 \times A_3$ describes the uncompensated topography and $A_1 \times A_2$ scales the compensated topography assuming Airy isostasy.

As evident from equation A_1, only the crust was considered to describe the uncompensated surface topography, or fossil figure, in the study. However, in the case of uncompensated topography from a fossil figure, both the top and bottom of the crust would be uplifted, implying that the mantle would also be uplifted below it. In addition, Garrick-Bethell et al. (2010) used the expression of Airy isostasy in Cartesian space for A_2, which is only an approximation for small bodies (see Dahlen, 1982; Hemingway & Matsuyama, 2017). By considering Airy isostasy as equal pressure in equal columns in spherical geometry, the aforementioned corrections revise the *A* constants to:

$$A_1 = \frac{5\bar{\rho}R}{3\rho_c + 3(\rho_m - \rho_c)\left(\frac{R-c}{R}\right)^4}; \;\; A_2 \times A_3 = 1 - \left(\frac{R-c}{R}\right)^4\frac{g_0}{g_m}$$

Using these, $H_{2,0,u}$ and $H_{2,2,u}$ are slightly reduced with respect to that found in Garrick-Bethell et al. (2010), and are -0.085 and 0.084 km instead of -0.114, and -0.111 km. We note that this slight difference has no effect on the conclusions presented in Garrick-Bethell et al. (2010), but have non-negligeable effects on our mare thickness estimation as discussed in the main text.

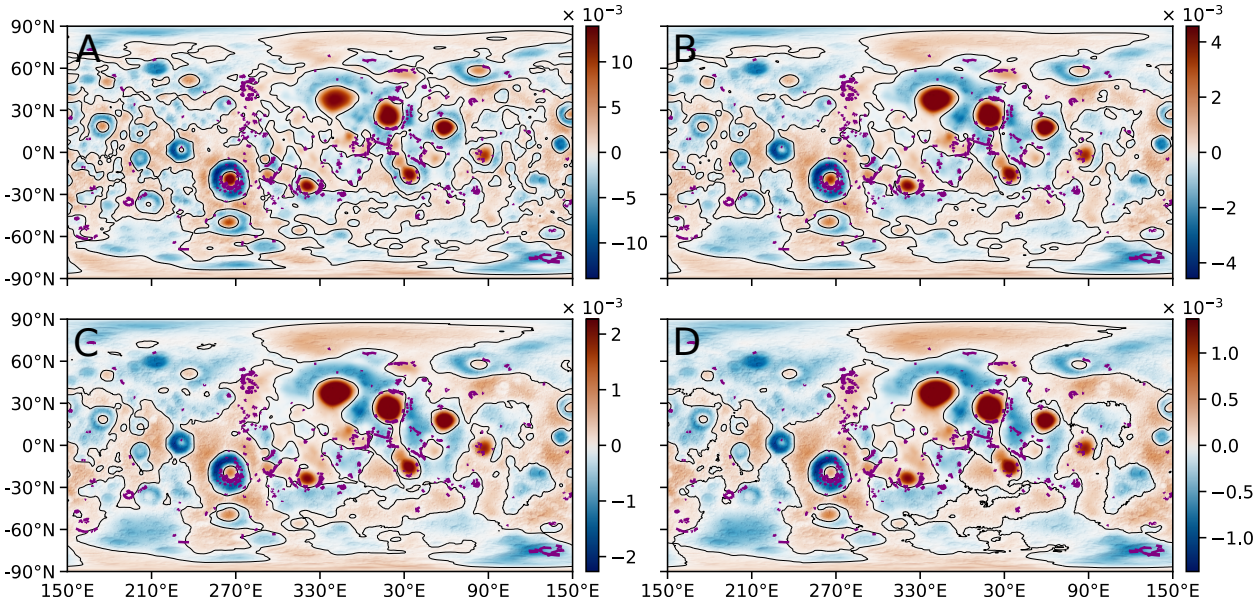

Figure S1: Global areal strain for elastic thicknesses of 20 (A), 40 (B), 60 (C), and 80 (D) km. Negative strains indicate extension. Note that extension is predicted close to Orientale (265°E - 20°N) for all elastic thicknesses due to the prominent crustal annulus loading. A black contour provide the zero-strain line. Negative strains indicate extension. Note the important change in strain magnitude as a function of elastic thickness.

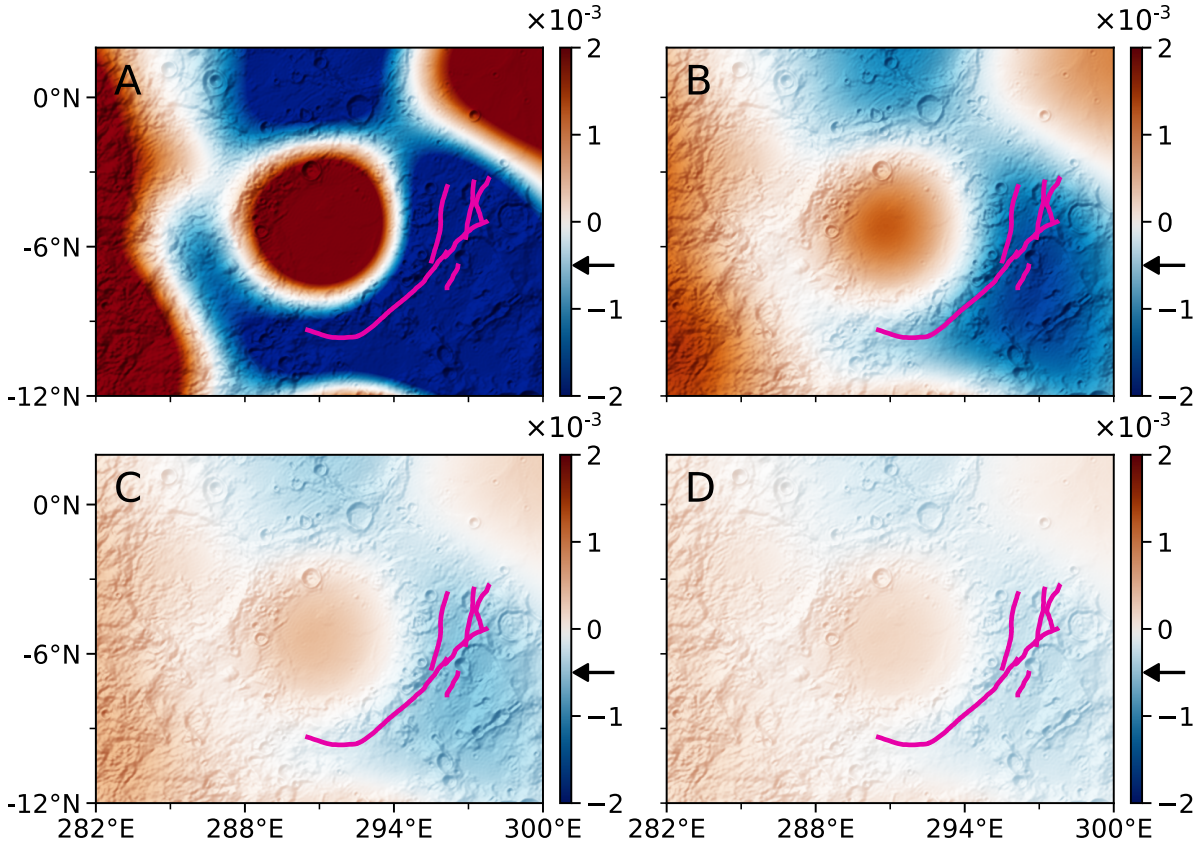

Figure S2: Areal strain fit to the tectonic record at Mare Grimaldi for elastic thicknesses of 20 (A), 40 (B), 60 (C), and 80 (D) km. Graben systems are indicated by the pink lines. The arrow on the color bar indicates an absolute tensile strain magnitude of 0.5×10^{-3} above which extensional tectonic failure would be favored.

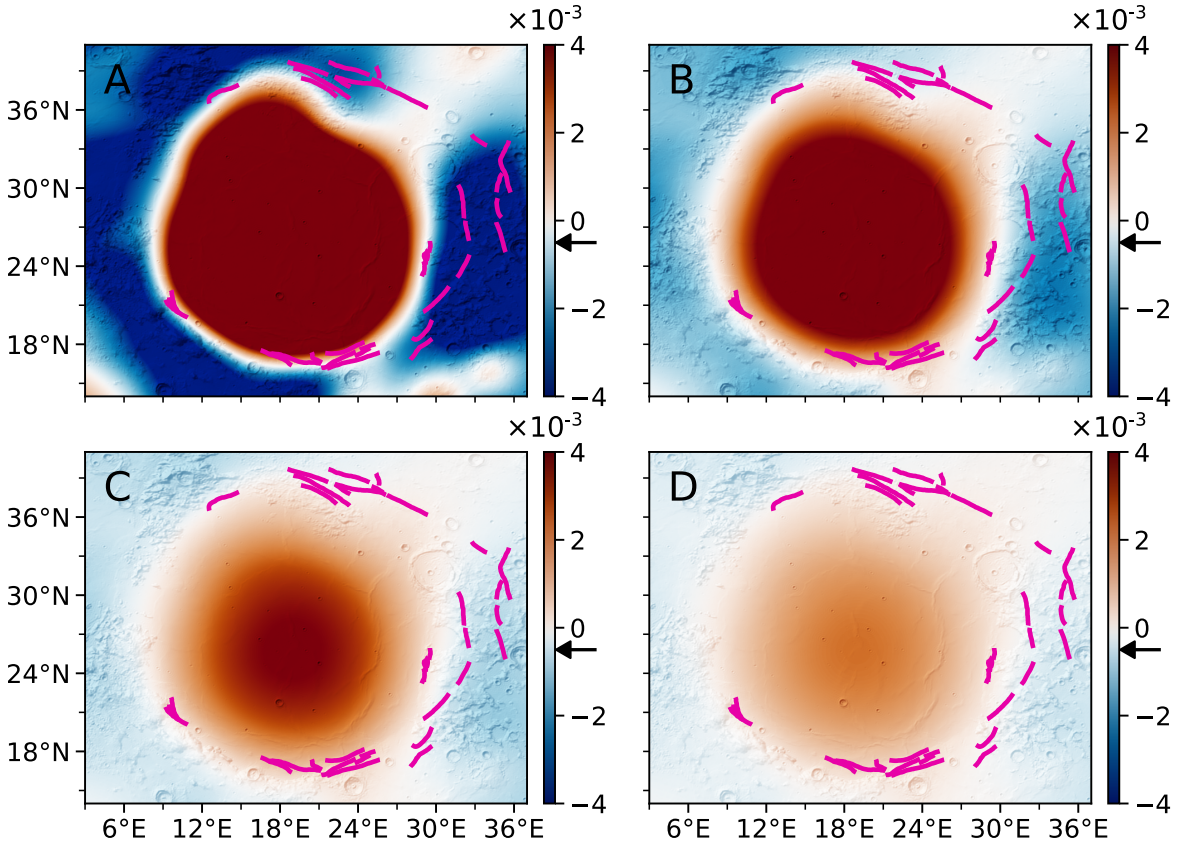

Figure S3: Areal strain fit to the tectonic record at Mare Serenitatis for elastic thicknesses of 20 (A), 40 (B), 60 (C), and 80 (D) km. The figure is the same format as Figure S2.

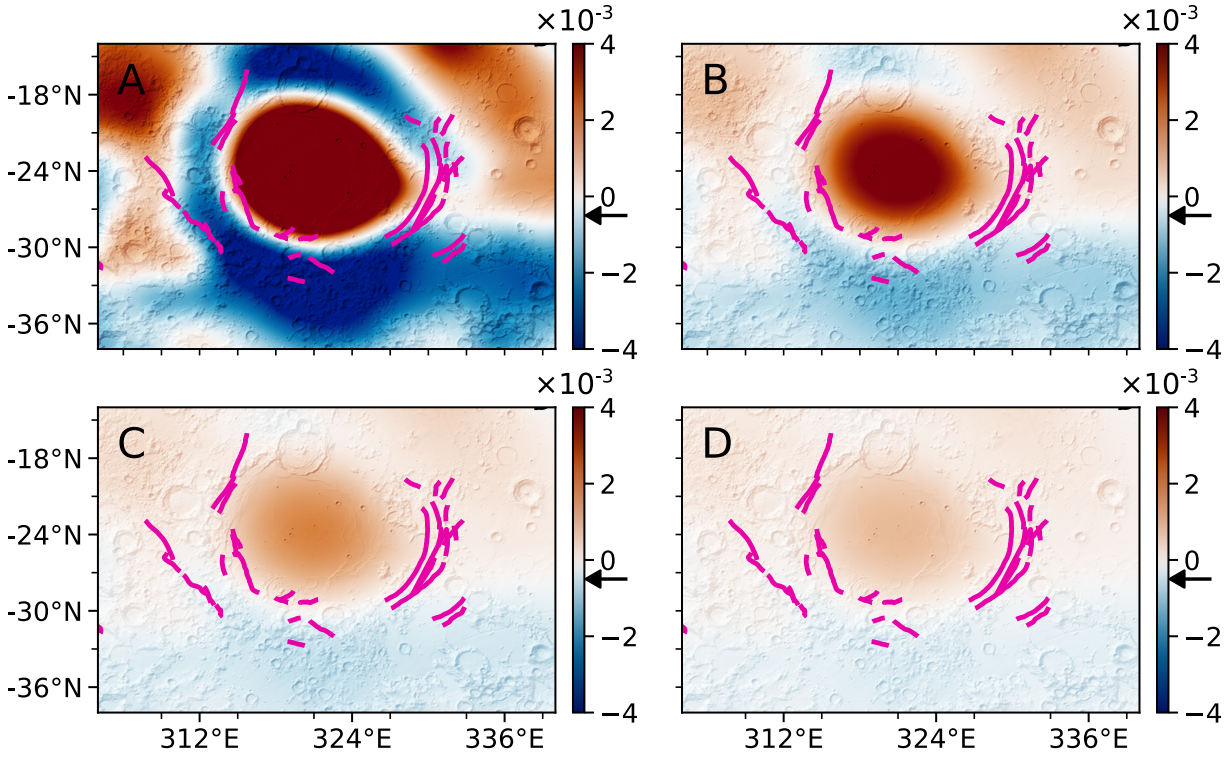

Figure S4: Areal strain fit to the tectonic record at Mare Humorum for elastic thicknesses of 20 (A), 40 (B), 60 (C), and 80 (D) km. The figure is the same format as Figure S2.

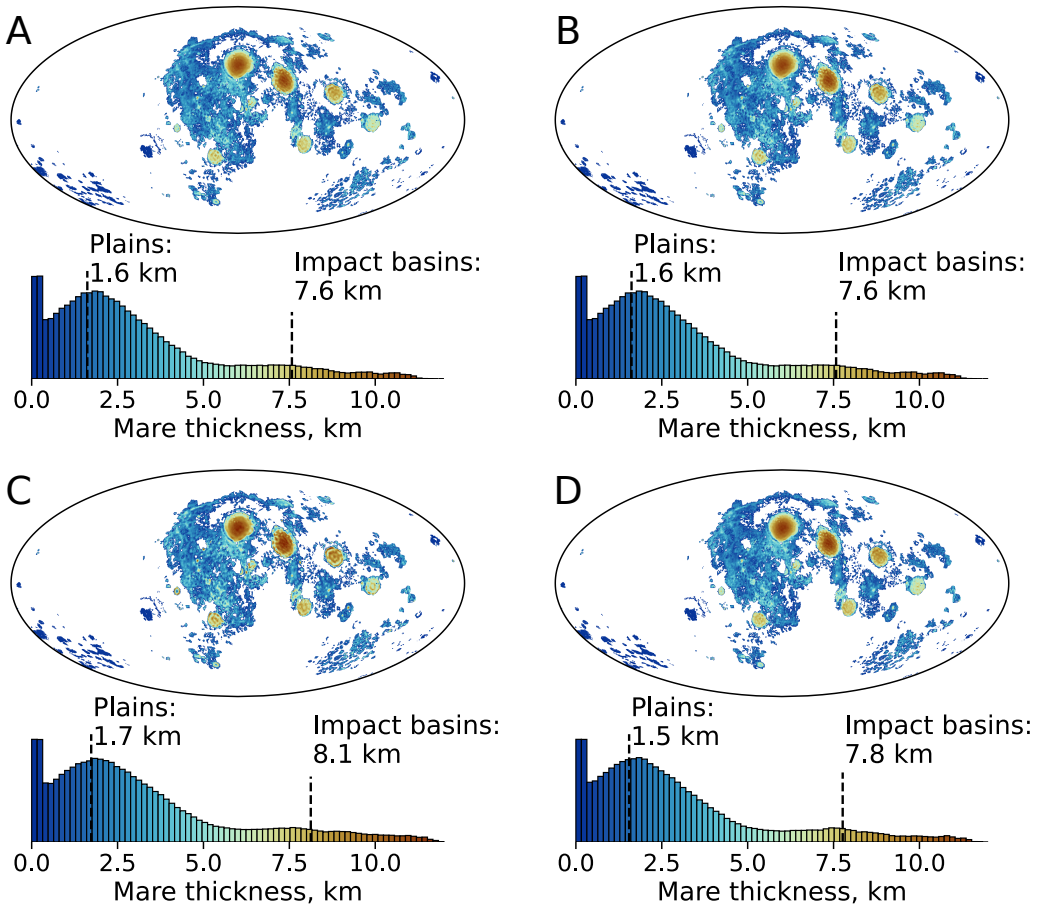

Figure S5: Mare thickness maps assuming an isostatic correction of ×1.1 (A) and ×0.9 (B) for the bottoms loads, and transition filters of 60–120 (C) and 110–170 (D) instead of our nominal 90–150. All models are consistent with that shown in Figure 3. The mare thickness model in C displays some ringing effects within Crisium, Nectaris and Humorum basins. This ringing is due to the mantle plug not being fully resolved for basins of a specific size (~350 km) in our estimation of the long-wavelength bottom loads, thereby propagating residual ringing effects to the mare top loads. When the filter starts at higher degrees, little no to ringing effect is observed. Such ringing effects are usually not observed in classical crustal thickness inversions, as the high degree moho relief is filtered out and discarded from the crustal thickness model (e.g., Wieczorek et al., 2013).

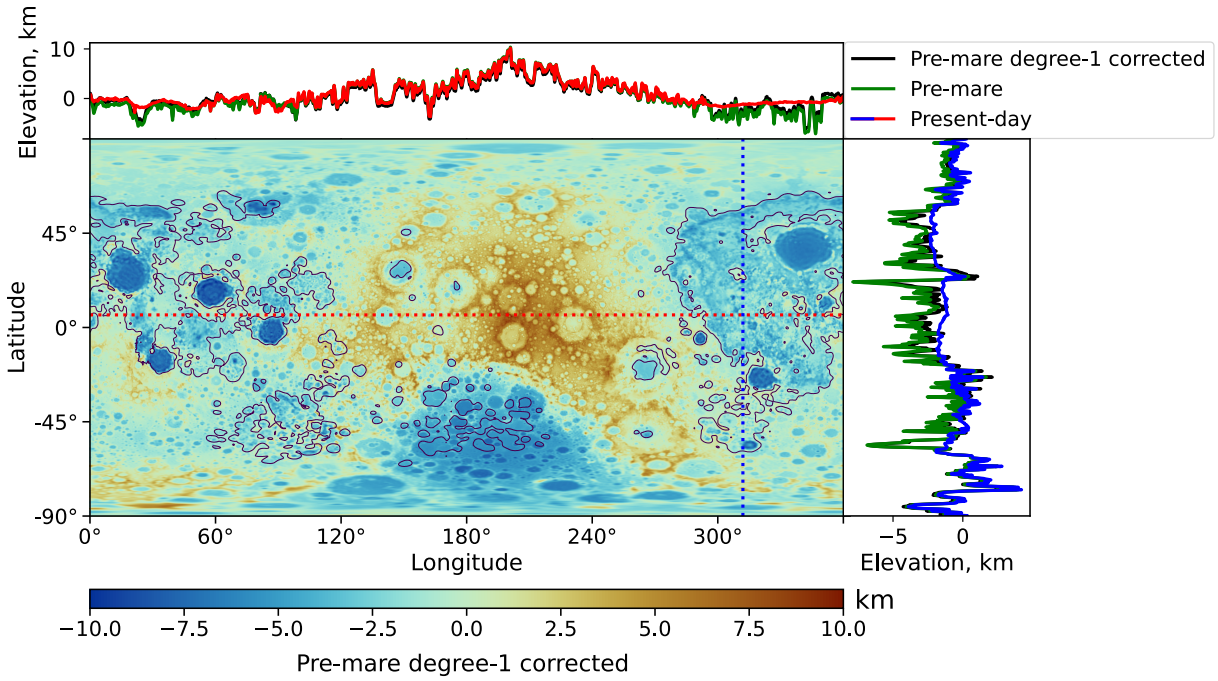

Figure S6: Pre-mare versus present-day topography and degree-1 correction. The central image displays the pre-mare topography (with the degree-1 correction) alongside east-west and north-south profiles for extracting elevation data, as shown in the upper and right panels. A purple contour indicates the extent of the mare units. The degree-1 correction induces a shift in elevation towards the nearside.

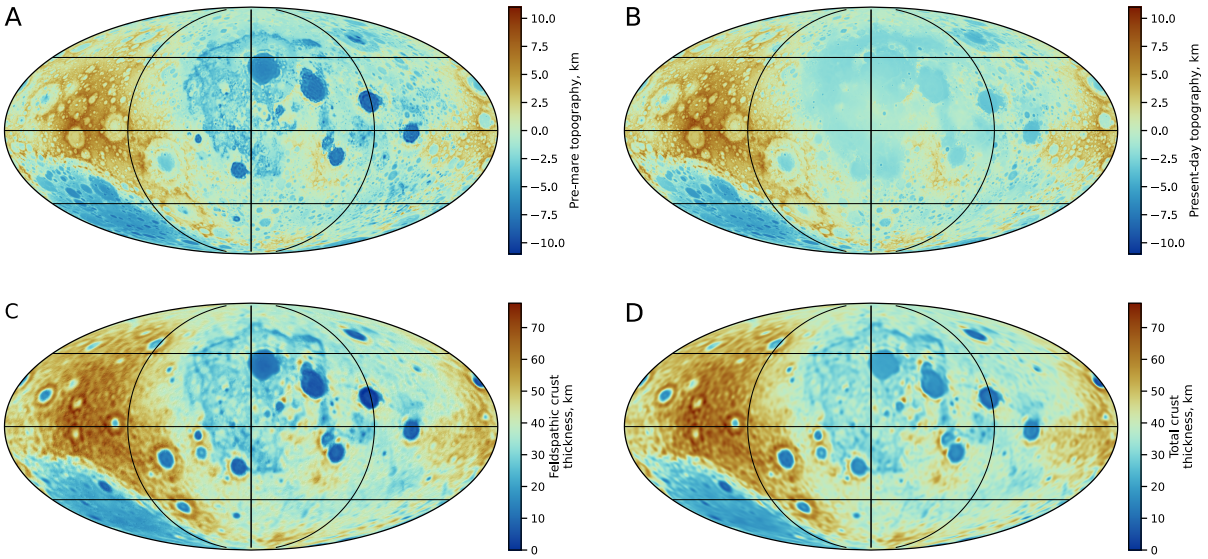

Figure S7: Pre-mare (A) versus present-day (B) topography, and pre-mare feldspathic (C) versus total (feldspathic + mare) (D) crustal thickness.

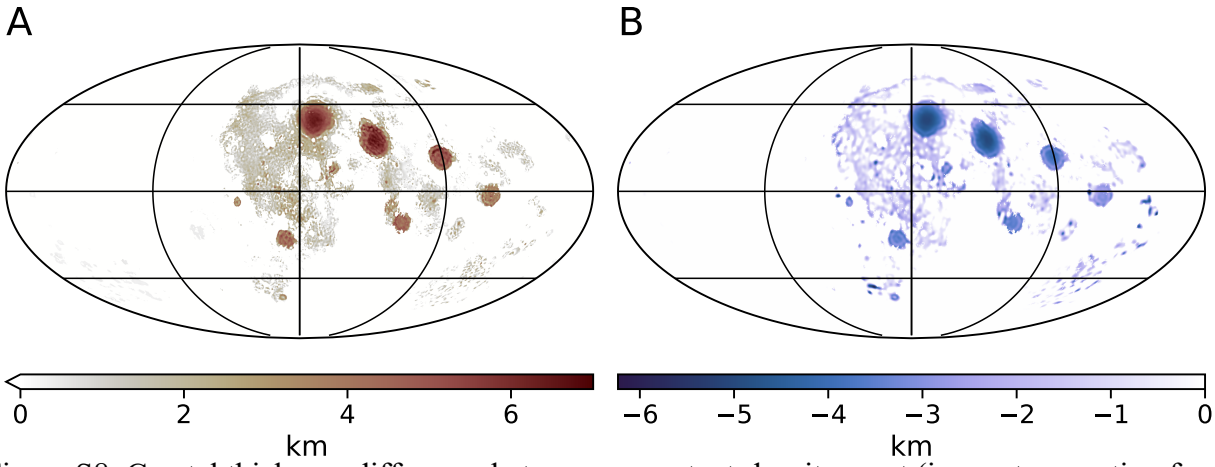

Figure S8: Crustal thickness difference between a constant-density crust (i.e., not correcting for the mare) and our estimated feldspathic crust thickness (A) and with respect to our total crustal thickness model (feldspathic + mare) (B).